

1 **Unraveling the Nature of Unidentified High Galactic Latitude *Fermi*/LAT**  
 2 **Gamma-ray Sources with *Suzaku***

3 K. Maeda<sup>1</sup>, J. Kataoka<sup>1</sup>, T. Nakamori<sup>1</sup>, Ł. Stawarz<sup>2,3</sup>, R. Makiya<sup>4</sup>, T. Totani<sup>4</sup>, C. C. Cheung<sup>5</sup>, D.  
 4 Donato<sup>6,7</sup>, N. Gehrels<sup>7</sup>, P. Saz Parkinson<sup>8</sup>, Y. Kanai<sup>9</sup>, N. Kawai<sup>9</sup>, Y. Tanaka<sup>2</sup>, R. Sato<sup>2</sup>, T.  
 5 Takahashi<sup>2</sup>, and Y. Takahashi<sup>1</sup>

6 ko-t.maeda.x-6@ruri.waseda.jp

7 **ABSTRACT**

8 Here we report on the results of deep X-ray follow-up observations of four unidentified  $\gamma$ -ray sources detected by the *Fermi*/LAT instrument at high Galactic latitudes using the X-ray Imaging Spectrometers on-board the *Suzaku* satellite. All of the studied objects were detected with high significance during the first 3-months of *Fermi*/LAT operation, and subsequently better localized in the first *Fermi*/LAT catalog (1FGL). For some of them, possible associations with pulsars and active galaxies have subsequently been discussed, and our observations provide an important contribution to this debate. In particular, a bright X-ray point source has been found within the 95% confidence error circle of 1FGL J1231.1–1410. The X-ray spectrum of the discovered *Suzaku* counterpart

---

<sup>1</sup>Research Institute for Science and Engineering, Waseda University, 3-4-1 Okubo, Shinjuku, Tokyo, 169-8555, Japan

<sup>2</sup>Institute of Space and Astronautical Science (ISAS), Japan Aerospace Exploration Agency (JAXA), 3-1-1 Yoshinodai, Chuo-ku, Sagami-hara, Kanagawa, 252-5510 Japan

<sup>3</sup>Astronomical Observatory, Jagiellonian University, ul. Orla 171, Kraków 30-244, Poland

<sup>4</sup>Department of Astronomy, Kyoto University, Kitashirakawa, Sakyo-ku, Kyoto, 606-8502, Japan

<sup>5</sup>NRC Research Associate, Space Science Division, Naval Research Laboratory, Washington, DC 20375, USA

<sup>6</sup>Center for Research and Exploration in Space Science and Technology (CRESST)

<sup>7</sup>NASA Goddard Space Flight Center, Greenbelt, MD 20771, USA

<sup>8</sup>Santa Cruz Institute for Particle Physics (SCIPP), University of California, Santa Cruz, Natural Sciences II, Room 313, 1156 High Street, Santa Cruz, CA 95064, USA

<sup>9</sup>Department of Physics, Tokyo Institute of Technology, 2-12-1, Ohokayama, Meguro, Tokyo, 152-8551, Japan

of 1FGL J1231.1–1410 is well fitted by a blackbody with an additional power-law component. This supports the recently claimed identification of this source with a millisecond pulsar PSR J1231–1411. For the remaining three *Fermi* objects, on the other hand, the performed X-ray observations are less conclusive. In the case of 1FGL J1311.7–3429, two bright X-ray point sources were found within the LAT 95% error circle. Even though the X-ray spectral and variability properties for these sources were robustly assessed, their physical nature and relationship with the  $\gamma$ -ray source remain uncertain. Similarly, we found several weak X-ray sources in the field of 1FGL J1333.2+5056, one coinciding with the high-redshift blazar CLASS J1333+5057. We argue that the available data are consistent with the physical association between these two objects, although the large positional uncertainty of the  $\gamma$ -ray source hinders a robust identification. Finally, we have detected an X-ray point source in the vicinity of 1FGL J2017.3+0603. This *Fermi* object was recently suggested to be associated with a newly discovered millisecond radio pulsar PSR J2017+0603, because of the spatial coincidence and the detection of the  $\gamma$ -ray pulsations in the light curve of 1FGL J2017.3+0603. Interestingly, we have detected the X-ray counterpart of the high-redshift blazar CLASS J2017+0603, located within the error circle of the  $\gamma$ -ray source, while we were only able to determine an X-ray flux upper limit at the pulsar position. All in all, our studies indicate that while a significant fraction of unidentified high Galactic latitude  $\gamma$ -ray sources is related to the pulsar and blazar phenomena, associations with other classes of astrophysical objects are still valid options.

9 *Subject headings:* galaxies: active — pulsars: general — radiation mechanisms: non-  
 10 thermal — gamma-rays: general — X-rays: general

## 11 **1. Introduction**

12 Observations with the EGRET instrument onboard the *Compton Gamma-Ray Observatory*  
 13 (CGRO) in the 1990’s opened a new window in studying MeV–GeV emissions from both Galactic  
 14 and extragalactic objects. Despite over a decade of multi-wavelength follow-up studies, more than  
 15 60% of the  $\gamma$ -ray emitters included in the 3rd EGRET catalog (3EG; Hartman et al. 1999) are  
 16 yet to be identified (that is, 170 out of 271). This is mainly because of the relatively poor  $\gamma$ -ray  
 17 localizations of EGRET sources (typical 95% confidence radii,  $r_{95} \simeq 0.4^\circ - 0.7^\circ$ ), challenging the  
 18 identification procedure especially for the objects located within the Galactic plane, due to source  
 19 confusion. In particular, as much as  $\simeq 90\%$  of the 3EG sources detected at Galactic latitudes  
 20  $|b| < 10^\circ$  do not have robustly selected counterparts at lower frequencies. On the other hand, most

21 of the 3EG sources at high Galactic latitudes have been associated with blazars — a sub-class of  
 22 jetted active galactic nuclei (AGN) displaying strong relativistic beaming — in accordance with  
 23 the expectation for the extragalactic population to dominate the  $\gamma$ -ray sky at  $|b| > 10^\circ$  (Abdo et al.  
 24 2009a). Yet the unidentified fraction of the high Galactic latitude 3EG sources is still large ( $\simeq 30\%$ ;  
 25 e.g., Sowards-Emmerd et al. 2003). The situation is basically unchanged in the revised EGRET  
 26 catalog (EGR; Casandjian & Grenier 2008), even though the revised background modeling applied  
 27 in the EGR resulted in fewer  $\gamma$ -ray detections (188 sources in total, in contrast to 271 listed in 3EG);  
 28 87 out of 188 EGR entries remain unidentified.

29 The unidentified low Galactic latitude  $\gamma$ -ray sources are expected to be associated with lo-  
 30 cal objects such as molecular clouds, supernova remnants, massive stars, pulsars and pulsar wind  
 31 nebulae, or X-ray binaries (see, e.g., Gehrels & Michelson 1999, and references therein). Mean-  
 32 while, the population of unidentified high Galactic latitude  $\gamma$ -ray sources is typically believed to  
 33 be predominantly extragalactic in origin, although there is a suspected Galactic component as  
 34 well (Özel & Thompson 1996). For example, the brightest steady source 3EG J1835+5918 lo-  
 35 cated at  $|b| > 10^\circ$  was proposed to be associated with an isolated neutron star (Mirabal et al.  
 36 2000; Reimer et al. 2001). The neutron star origin and its association with the  $\gamma$ -ray source has  
 37 been confirmed with the discovery of a  $\gamma$ -ray pulsar at the position of 3EG J1835+5918 with  
 38 *Fermi*/LAT (Abdo et al. 2010a,b). Similarly, high-energy  $\gamma$ -ray pulsations were discovered with  
 39 *Fermi* (Abdo et al. 2009b) and *AGILE* (Tavani et al. 2009) from PSR J2021+3651 that was long  
 40 considered as a likely pulsar counterpart of 3EG J2021+3716 (Halpern et al. 2008). On the other  
 41 hand, blazar G74.87+1.22 (B 2013+370) was claimed to be the most likely counterpart of the  
 42 unidentified object 3EG J2016+3657 located within the Galactic plane (Mukherjee et al. 2000;  
 43 Halpern et al. 2001). Other unidentified  $\gamma$ -rays sources were similarly investigated with varying  
 44 success (e.g., Mukherjee & Halpern 2004). We note that population studies, which could in princi-  
 45 ple shed some light on the galactic/extragalactic origin of different classes of unidentified EGRET  
 46 sources, were impeded by different level of background emission at different locations from the  
 47 Galactic plane, and different EGRET exposure for various parts of the sky (see the discussion in  
 48 Reimer 2001). Also, variability studies were previously hampered by the limited statistics and  
 49 noncontinuous EGRET observations (Nolan et al. 2003).

50 With the successful launch of the *Fermi* Gamma-ray Space Telescope, we now have a new op-  
 51 portunity to study  $\gamma$ -ray emission from different types of high energy sources with much improved  
 52 sensitivity and localization capabilities than with EGRET. With its field of view (five-times-larger  
 53 than that of EGRET) covering 20% of the sky at every moment, and its improved sensitivity  
 54 (by more than an order of magnitude with respect to EGRET), the Large Area Telescope (LAT;  
 55 Atwood et al. 2009) aboard *Fermi* surveys the entire sky each day down to a photon flux lev-  
 56 els of  $F_{>100\text{MeV}} \simeq \text{few} \times 10^{-7} \text{ ph cm}^{-2} \text{ s}^{-1}$ . The first *Fermi*/LAT point source catalog (1FGL)  
 57 already surpasses EGRET with 1451 sources detected at significance levels  $> 4\sigma$  within the

58 100 MeV – 100 GeV photon energy range during the initial 11-month survey (Abdo et al. 2010c).  
 59 Several high-latitude EGRET sources lacking low-frequency counterparts were confirmed by *Fermi*/LAT  
 60 and associated with previously unknown  $\gamma$ -ray blazars, as expected (Abdo et al. 2010d). Somewhat  
 61 surprisingly, however, a number of  $\gamma$ -ray emitters at  $|b| > 10^\circ$  have been robustly identified by LAT  
 62 with newly found  $\gamma$ -ray pulsars via the detection of  $\gamma$ -ray pulsations (Abdo et al. 2010e). Most of  
 63 these are in fact millisecond pulsars (MSPs). A diminishing, yet still significant population of  
 64 unidentified *Fermi*/LAT objects remains, constituting as much as about 40% of all 1FGL sources.  
 65 This includes more than 10 unidentified EGRET sources at high Galactic latitudes, which are thus  
 66 the best candidates for the persistent, or even “steady”  $\gamma$ -ray emitters over the 10-year-long period  
 67 between the EGRET and *Fermi*/LAT epochs (as indicated by their comparable photon fluxes in the  
 68 3EG and 1FGL catalogs).

69 Thus motivated, we started a new project to investigate the nature of unidentified high Galactic  
 70 latitude *Fermi* objects through deep X-ray follow-up observations with the Japanese X-ray astron-  
 71 omy satellite *Suzaku* (Mitsuda et al. 2007). This paper presents the results of the first year cam-  
 72 paign conducted over the span of *Suzaku*-AO4 (Apr 2009 – Mar 2010), during which we have ob-  
 73 served four steady/weakly variable *Fermi*/LAT sources from the 3-month *Fermi*/LAT Bright Source  
 74 List (0FGL; Abdo et al. 2009c). These are denoted below accordingly to their 1FGL catalog en-  
 75 tries as 1FGL J1231.1–1410, 1FGL J1311.7–3429, 1FGL J1333.2+5056, and 1FGL J2017.3+0603.  
 76 Thanks to the superb localization provided by the LAT, all the corresponding 95% error cir-  
 77 cles (typically  $r_{95} \simeq 0.1^\circ - 0.2^\circ$ ) could be covered within the field-of-view of the *Suzaku* X-  
 78 ray CCD camera “XIS”. Only in the case of 1FGL J1333.2+5056, the *Suzaku* pointing does  
 79 not cover the entire 95% LAT error circle since the localization error for this object did not  
 80 improve sufficiently between 1FGL and 0FGL. Along with our *Suzaku* observations, system-  
 81 atic pulsar searches with radio telescopes have been performed for the *Fermi*/LAT unassociated  
 82 sources. These resulted in the new discoveries of MSPs co-located with the two  $\gamma$ -ray sources  
 83 included in our study (1FGL J1231.1–1410 and 1FGL J2017.3+0603). In both cases, *Fermi*/LAT  
 84 eventually detected  $\gamma$ -ray pulsations as well, in accordance with the results in the radio domain  
 85 (Ransom et al. 2010; Cognard et al. 2010). Our deep X-ray exposure discussed in the next sec-  
 86 tions supports the pulsar identification for at least 1FGL 1231.1–1410, but is less conclusive in the  
 87 case of 1FGL J2017.3+0603. For the other target from our list, 1FGL J1333.2+5056, a tentative  
 88 association with blazar CLASS J1333+5057 was claimed in the LAT Bright AGN Sample (LBAS;  
 89 Abdo et al. 2009a). Here we substantiate this possibility by presenting the broad-band spectral en-  
 90 ergy distribution (SED) for 1FGL J1333.2+5056/CLASS J1333+5057, including new *Suzaku* data,  
 91 which is indeed typical of a flat spectrum radio quasar (FSRQ). Finally, the nature of the remain-  
 92 ing source 1FGL J1311.7–3429 (for which no radio or  $\gamma$ -ray pulsations have been detected so far;  
 93 Ransom et al. 2010) could not be revealed, despite the discovery of a likely X-ray counterpart. In  
 94 particular, we found that the multiwavelength spectrum of 1FGL J1311.7–3429 is not consistent

95 with neither a typical blazar nor pulsar spectrum.

96 In § 2, we describe the *Suzaku* X-ray follow-up observations and the data reduction procedure.  
 97 The results of the analysis are given in § 3. The discussion and conclusions are presented in § 4  
 98 and § 5, respectively. A standard  $\Lambda$ CDM cosmology with  $\Omega_\Lambda = 0.73$ ,  $\Omega_M = 0.27$ , and  $H_0 =$   
 99  $71 \text{ km s}^{-1} \text{ Mpc}^{-1}$  is assumed throughout the paper.

## 100 2. Observations and Analysis

### 101 2.1. Observations and Data Reduction

102 We observed four unidentified high Galactic latitude *Fermi*/LAT objects with the *Suzaku* X-  
 103 ray astronomy satellite (Mitsuda et al. 2007). These are denoted in the 1FGL catalog as 1FGL J1231.1–  
 104 1410, 1FGL J1311.7–3429, 1FGL J1333.2+5056, and 1FGL J2017.3+0603 (see Abdo et al. 2010c).  
 105 All the sources but one (1FGL J2017.3+0603) were already listed in the 3rd EGRET catalog  
 106 (Hartman et al. 1999) and their  $\gamma$ -ray fluxes are given in Table 1. The *Suzaku* observation logs  
 107 are summarized in Table 2. The observations were made with three out of four CCD cameras  
 108 (X-ray Imaging Spectrometers; XIS; Koyama et al. 2007), and a Hard X-ray Detector (HXD;  
 109 Kokubun et al. 2007; Takahashi et al. 2007). One of the XIS sensors is a back-illuminated CCD  
 110 (BI; XIS1), and the other three XIS sensors are front-illuminated ones (FI; XIS0, XIS2, and XIS3;  
 111 the operation of XIS2 has been terminated in November 2006). Since none of the studied sources  
 112 have been detected with the HXD, in this paper we focus on the analysis of only the XIS data.  
 113 The XIS was operated in the pointing source mode and in the normal clocking mode during all the  
 114 exposures.

115 In the reduction and the analysis of the *Suzaku* data, HEADAS software version 6.7 and a  
 116 calibration database (CALDB; released on 2009 September 25th) were used. The XIS cleaned  
 117 event dataset was obtained in the combined  $3 \times 3$  and  $5 \times 5$  edit modes using `xselect`. We  
 118 excluded the data collected during the time and up to 60 seconds after *Suzaku* was passing the South  
 119 Atlantic Anomaly (SAA). We also excluded the data corresponding to less than 5 degrees of the  
 120 angle between the Earth’s limb and the pointing direction (the Elevation Angle; ELV). Moreover,  
 121 we excluded time windows during which the spacecraft was passing through the low Cut-Off  
 122 Rigidity (COR) of below 6 GV. Finally, we removed hot and flickering pixels (using `sisclean`;  
 123 Day et al. 1998). With all the aforementioned data selection criteria applied, the resulting total  
 124 effective exposures for all the observed sources are summarized in Table 2.

125

## 2.2. Analysis

126 XIS images for each target were extracted from the two FI CCDs (XIS0, XIS3) within the  
 127 photon energy range from 0.4 to 10 keV. In the image analysis procedure, calibration sources lo-  
 128 cated at the corners of CCD chips were excluded. The images of Non X-ray Background (NXB)  
 129 were obtained from the night Earth data using `xisnxbgen` (Tawa et al. 2008). Since the expo-  
 130 sure times for the original data were different from that of NXB, we calculated the appropriate  
 131 exposure-corrected original and NXB maps using `xisexppmapgen` (Ishisaki et al. 2007). The  
 132 corrected NXB images were next subtracted from the corrected original images. In addition, we  
 133 simulated flat sky images using `xissim` (Ishisaki et al. 2007), and applied a vignetting correction.  
 134 All the images obtained with XIS0 and XIS3 were combined and re-binned by a factor of 4. All  
 135 the FI XIS images were in addition smoothed by a Gaussian function with  $\sigma = 0.17$ , and the  
 136 resultant images are presented in section 3. Note that the apparent features at the edge of these  
 137 exposure corrected images are undoubtedly spurious due to low exposure in those regions. For the  
 138 further analysis, source regions were carefully selected around each detected X-ray sources within  
 139 the error circle of a studied  $\gamma$ -ray emitter. The corresponding background regions with radius  $3'$   
 140 were taken from the same XIS chips avoiding any bright X-ray spots in the field. In all the cases,  
 141 such source regions were set to within  $3'$  or  $1'$  radii around the X-ray point sources (because of  
 142 the blurring due to the *Suzaku*/XIS Point Spread Function; PSF), depending on the properties of  
 143 each analyzed field. The source detection criterion was based on a signal-to-noise ratio which is  
 144 defined, assuming a Poisson distribution, as a ratio of the excess events above a background to its  
 145 standard deviation. Photon counts were derived from each source and background regions and we  
 146 set the detection threshold at  $4\sigma$ . The source positions and the corresponding errors were obtained  
 147 by fitting a 2D Gaussian around each X-ray spot. The source detection results are summarized in  
 148 Table 3.

149 The light curves were constructed for each potential X-ray counterpart of the observed *Fermi*  
 150 objects. Each light curve provides net-counting rates, with the count rates of the corresponding  
 151 background region subtracted. In the timing analysis, the FI (XIS0, XIS3) and BI (XIS1) CCD's  
 152 light curves were combined using `lcmath`, and then re-binned using `lcurve`. To assess statisti-  
 153 cal significances of the flux variations, the  $\chi^2$  test was applied to each constructed dataset (probing  
 154 a constant flux hypothesis with `lcstats` command). Finally, the XIS spectra for each source  
 155 region were extracted, with the same corresponding background spectra as defined in the image  
 156 analysis (see above). RMF files for the detector response and ARF files for the effective area were  
 157 generated using `xisrmfgen` and `xissimarfgen` (Ishisaki et al. 2007). In this spectral analy-  
 158 sis, all the selected data from the FI CCDs were co-added (using `mathpha`) without calculating  
 159 Poisson errors, and the response files were combined with the `marfrmf` and `addrmf` commands.  
 160 Since all the studied *Fermi*/LAT objects are located at high Galactic latitudes, the absorption of

161 soft X-ray photons was set to the Galactic one with the equivalent column density of a neutral  
 162 hydrogen,  $N_{\text{H}}$ , as given in Dickey & Lockman (1990). In some cases where apparent systematic  
 163 features are visible as trends of the residuals with energy (see Figure 3), we attempted to use an  
 164 inter-calibration constant between the FI and BI CCDs to improve the fits. From this inspection,  
 165 we found negligible improvement of the fits thus we conclude that the limited photon statistics is  
 166 the predominantly responsible for the somewhat unsatisfactory model fits to the data.

### 167 3. Results

#### 168 3.1. 1FGL J1231.4–1410

169 Our *Suzaku* observations (interrupted for  $\simeq 20$  days<sup>1</sup>) revealed one X-ray point source (RA,  
 170 Dec) = (187.<sup>o</sup>790(1),  $-14.$ <sup>o</sup>192(1)) within the LAT error circle of 1FGL J1231.4–1410. Figure 1  
 171 shows the corresponding X-ray image, prepared as described in § 2.2. For further analysis, the  
 172 source extraction region was set to within a 3' radius around the X-ray intensity peak, and the  
 173 corresponding background region was chosen as indicated in Figure 1. The light curve of the X-  
 174 ray source with a time bin of 900 s is presented in Figure 2. The upper panel shows the count rate  
 175 variation during the 1st observation, while the bottom panel shows that of the 2nd observation. The  
 176 light curves of the two periods can both be well fitted by a constant count rate of  $3.03 \times 10^{-2}$  ct s<sup>-1</sup>,  
 177 with  $\chi^2/\text{d.o.f.} = 58.3/107$ . This indicates that the X-ray emission of the analyzed source is steady,  
 178 with the  $\chi^2$  probability for a constant flux  $> 99\%$ .

179 The X-ray spectrum of the *Suzaku* source, which we propose to be the most likely counterpart  
 180 of 1FGL J1231.1–1410, is shown in Figure 3. The energy range used for the fitting was set as  
 181 0.4 – 7.0 keV. First, we fit the X-ray spectrum by a blackbody emission moderated by the Galactic  
 182 absorption only (Morrison & McCammon 1983). This fit was not acceptable, however, due to  
 183 significant residuals above 2 keV ( $\chi^2/\text{d.o.f.} = 128.1/34$ , see Figure 3, left panel, where the excess  
 184 emission above 2 keV has been enhanced by fixing the black body parameters to those determined  
 185 by the data below 2 keV only). The situation was essentially unchanged when the column density  
 186 was treated as a free parameter. In this case, the residuals above 2 keV remained, but the returned  
 187 value of  $N_{\text{H}}$  was then consistent with zero. To account for the  $> 2$  keV emission, we therefore  
 188 added a power-law component to the thermal one, and fixed  $N_{\text{H}} = 0$ . The goodness of the fit was  
 189 in this way substantially improved to  $\chi^2$  of 55.46/32, supporting the presence of a non-thermal tail  
 190 in the spectrum of the analyzed object (see Figure 3). In order to further confirm the reality of this  
 191 finding, we analyzed the highest quality FI CCD (XIS0, XIS3) data which had sufficient photon

---

<sup>1</sup>The exposure was interrupted because of the Target of Opportunity observation of GRB 090708.

192 statistics within the 2 – 8 keV range, examining various approaches for the background estimation,  
 193 namely (i) the background taken from the same CCD chips but off-axis, as given in Figure 1, (ii)  
 194 the concentric ring background surrounding the source region on the same CCD chips, and (iii) the  
 195 background for the same region as the source estimated from the Lockman Hole observation taken  
 196 with the same XIS mode at nearby dates (OBS ID = 104002010). In all of the examined approaches  
 197 the presence of the non-thermal component in the X-ray spectrum of 1FGL J1231.1–1410 could  
 198 be confirmed at high significance, as summarized in Tables 4 and 5.

199 To sum up, we conclude that the X-ray counterpart of 1FGL J1231.1–1410 is robustly charac-  
 200 terized by a blackbody-type spectrum with a temperature of  $kT \simeq 0.16 \pm 0.03$  keV plus a power-  
 201 law tail with the photon index of  $\Gamma \simeq 1.79_{-0.17}^{+0.40}$ . The energy flux of the non-thermal component  
 202 is  $S_{2-8\text{ keV}} \simeq 5.81 \times 10^{-14}$  erg cm $^{-2}$  s $^{-1}$ , which can be compared with the *Fermi*/LAT energy flux  
 203  $S_{0.1-10\text{ GeV}} \simeq (1.06 \pm 0.06) \times 10^{-10}$  erg cm $^{-2}$  s $^{-1}$ , as given in the 1FGL catalog. Thus, the extrap-  
 204 olation of the X-ray power-law component to the  $\gamma$ -ray range yielding the 0.1 – 10 GeV energy  
 205 flux  $\simeq 5.74 \times 10^{-13}$  erg cm $^{-2}$  s $^{-1}$ , falls orders of magnitudes below the observed one. This implies  
 206 either a multi-component character or a concave spectral form of the high-energy X-ray-to- $\gamma$ -ray  
 207 continuum of 1FGL J1231.1–1410, and both possibilities should be kept in mind in the context of  
 208 a very likely association of the discussed source with a MSP. Indeed, the MSP PSR J1231–1411  
 209 (marked by a white cross in Figure 1) was recently found by Ransom et al. (2010) via the detection  
 210 of radio pulsations with the pulse period of 3.68 ms within the LAT error circle of 1FGL J1231.1–  
 211 1410 using the Green Bank Telescope (GBT), just after our *Suzaku* observations. In addition, the  
 212 *Fermi* spectrum shows a cut-off at around a few GeV, which is consistent with the typical spec-  
 213 trum of MSPs (Ransom et al. 2010). The X-ray emitter observed by *Suzaku* is located roughly  
 214 40'' away from the newly discovered MSP PSR J1231–1411 (Ransom et al. 2010, see Figure 1),  
 215 but considering the limited pointing accuracy of the *Suzaku*/XIS ( $\lesssim 1'$ ), both objects can be con-  
 216 sidered as co-spatial. In fact, as described in Ransom et al. (2010), a *Swift*/XRT source at (RA,  
 217 Dec) = (187.7972, –14.1953) coinciding with the *Suzaku* one, was found to be positionally con-  
 218 sistent (within the 90% error of 5.''5) with that of the MSP PSR J1231–1411.

### 219 3.2. 1FGL J1311.7–3429

220 Two X-ray point sources were found within the LAT error circle of 1FGL J1311.7–3429.  
 221 Figure 4 shows the corresponding X-ray image with the northern *Suzaku* object, src A, located  
 222 at (RA, Dec) = (197.°939(1), –34.°508(2)) and the southern source, src B, positioned at (RA,  
 223 Dec) = (197.°942(1), –34.°534(2)). Note that src B is situated just marginally within the edge  
 224 of the *Fermi*/LAT error circle. For the further analysis, we set the source regions to within 1' radii  
 225 around the respective X-ray flux maxima. The derived light curves of src A and src B with time



bins of 450 s are presented in Figure 5 (upper and lower panels, respectively). As shown, during the first 20 ksec of the observation, src A exhibited a very rapid X-ray flare, with the count rate changing by a factor of 10. After the flare, however, the X-ray flux of src A remained steady. A constant fit to the light curve of src A returns  $\chi^2/\text{d.o.f.} = 403.9/97$ , and hence the variability of this source is statistically significant. On the other hand, src B was characterized by a constant flux over the duration of the exposure ( $\chi^2/\text{d.o.f.} = 45.0/97$ ) with a count rate of  $1.3 \times 10^{-2} \text{ ct s}^{-1}$ .

Figure 6 shows the spectra of src A and src B within the energy range 0.4 – 8.0 keV. The best model fits for both newly discovered X-ray objects consist of power-law continua with photon indices  $\Gamma \simeq 1.38 \pm 0.13$  (src A) and  $\Gamma \simeq 1.34 \pm 0.16$  (src B), moderated by the Galactic absorption. The detail of the model fitting are summarized in Table 6. Note that the observed X-ray spectra of the two sources are very similar, and the X-ray fluxes of the objects are almost identical. It is important to emphasize at this point that because of the relatively large PSF of *Suzaku*/XIS (a half power diameter of  $\sim 3'$ ), it is quite difficult to separate completely src A and src B — located only  $1.6'$  apart — for the purpose of the spectral analysis. As a result, even though it is clear we are dealing with two physically distinct X-ray sources (each detected at high significance), their spectral parameters cannot be accessed robustly.

### 3.3. 1FGL J1333.2+5056

Our *Suzaku* observations revealed multiple regions of enhanced X-ray emission inside the LAT error circle of 1FGL J1333.2+5056, as shown in the corresponding X-ray image in Figure 7. The associations of these faint X-ray sources with 1FGL J1333.2+5056 are therefore quite ambiguous. Within the *Fermi*/LAT error circle covered by the XIS exposure<sup>2</sup>, five X-ray enhancements have been found with detection significances of more than  $4\sigma$ , and these are denoted here as src A, B, C, D and E (see Figure 7 and Table 3).

The light curves of src A, B, C, D and E with 5760 s binning are shown in Figure 8 in the descending order. As noted above, all the analyzed X-ray sources are very dim, with X-ray fluxes at the level of  $\sim 10^{-14} \text{ erg cm}^{-2} \text{ s}^{-1}$ . Hence, we could not assess the variability properties of the selected objects by means of the  $\chi^2$  test with a constant flux hypothesis (see Table 7). The spectra of the five X-ray sources, all extracted within  $1'$  source radii, are shown in Figure 9. Again, limited photon statistics precluded any detailed analysis, and therefore in the model fitting we applied only single power-law models moderated by the Galactic absorption. The results are summarized

---

<sup>2</sup>Note that the 1FGL localization error for the analyzed  $\gamma$ -ray object did not improve sufficiently between 0FGL and 1FGL. For this reason, we could not cover the entire 95% LAT error circle of 1FGL J1333.2+5056 within one pointing of *Suzaku*/XIS.

256 in Table 8. We also emphasize that the 1FGL error circle unfortunately runs off the edge of *Suzaku*  
 257 field of view. For all these reasons, we cannot persuasively identify an X-ray counterpart of the  $\gamma$ -  
 258 ray source 1FGL J1333.2+5056. Nevertheless, we note that one of the X-ray enhancements, src D,  
 259 coincides with the  $z = 1.362$  FSRQ CLASS J1333+5057 (marked in Figure 7 by a white cross;  
 260 Shaw et al. 2009), listed in the 1FGL as a possible association with 1FGL J1333.2+5056. Note  
 261 however a relatively low significance of the detection of this source with *Suzaku*/XIS.

### 262 3.4. 1FGL J2017.3+0603

263 A single prominent X-ray point source was found at the edge of the 1FGL error circle of  
 264 the unidentified  $\gamma$ -ray source 1FGL J2017.3+0603. The X-ray source is located at (RA, Dec) =  
 265 (304. $^{\circ}$ 310(1), 6. $^{\circ}$ 052(1)), as shown in Figure 10. For the further analysis, we set the extraction  
 266 region to encircle this bright source with a radius of 3'. The corresponding light curve of the newly  
 267 discovered X-ray source is show in Figure 11 with 620 s binning. The light curve is consistent (at  
 268 the level of > 99%) with a constant X-ray flux within the errors ( $\chi^2/\text{d.o.f.} = 26.4/56$ ) and the  
 269 average count rate  $4.07 \times 10^{-2} \text{ ct s}^{-1}$ . Figure 12 shows the X-ray spectrum of the analyzed source.  
 270 A power-law model (photon index  $\Gamma \simeq 1.6$ ) with the Galactic absorption provided the best fit to  
 271 the data, and the obtained best fit parameters are given in Table 9.

272 The X-ray point source found at the edge of the 1FGL error circle is positionally coincident  
 273 (offset by 15'', which is much less the *Suzaku*/XIS position accuracy of  $\sim 1'$ ) with the  $z = 1.743$   
 274 FSRQ CLASS J2017+0603 (Myers et al. 2003). This blazar has been listed in the first *Fermi*/LAT  
 275 AGN Catalog (Abdo et al. 2010d) as being possibly associated with 1FGL J2017.3+0603, even  
 276 though the probability for such an association was not quantified. We denote its position in Fig-  
 277 ure 10 with a white cross. More recently, radio and  $\gamma$ -ray pulsations with the pulse period of 2.9 ms  
 278 have been discovered using the Nancay radio telescope well within the *Fermi*/LAT error circle of  
 279 1FGL J2017.3+0603 (Cognard et al. 2010), pointing instead to a pulsar (rather than blazar) as-  
 280 sociation of this source. In Figure 10 we mark the position of the MSP PSR J2017+0603 with  
 281 a black cross. As shown, no X-ray counterpart of the pulsar has been detected by *Suzaku*/XIS.  
 282 In order to determine the corresponding X-ray flux upper limit, we set an additional source re-  
 283 gion within 1' radius around the position of the radio pulsar, and assumed a power-law emis-  
 284 sion spectrum with photon index  $\Gamma = 2$ . The resulting 90% confidence X-ray upper limit is  
 285  $S_{2-8 \text{ keV}} < 2.61 \times 10^{-14} \text{ erg cm}^{-2} \text{ s}^{-1}$ .

286

## 4. Discussion

287

### 4.1. The Observed Sample

288 Within the error circle of the unidentified  $\gamma$ -ray object 1FGL J1231.4–1410, only one X-ray  
 289 source was found, which is positionally consistent with the radio/ $\gamma$ -ray MSP PSR J1231–1411  
 290 (Ransom et al. 2010, see Figure 1). The broad band spectrum of 1FGL J1231.1–1410/PSR J1231–  
 291 1411, including our *Suzaku*/XIS data and the derived UVOT optical/UV upper limits from *Swift*,  
 292 are shown in Figure 13. We note that the SED is reminiscent of that of the Geminga pulsar  
 293 (Thompson et al. 1999), or 3EG J1835+5918 (Halpern et al. 2002). Hence the consistent picture  
 294 emerges, in which the  $kT \simeq 0.16$  keV blackbody component of the newly discovered X-ray coun-  
 295 terpart of 1FGL J1231.1–1410 originates as thermal emission from the surface of a rotating mag-  
 296 netized neutron star, a pulsar, while the  $\gamma$ -ray emission detected by *Fermi*/LAT may be accounted  
 297 by the emission of ultra-relativistic electrons present within the pulsar magnetosphere. The non-  
 298 thermal X-ray component is then likely to be produced within the magnetosphere of PSR J1231–  
 299 1411 as well, even though one may also expect some contribution from the outer regions (pulsar  
 300 wind nebulae) to the detected hard X-ray continuum.

301 Assuming that PSR J1231–1411 is a typical MSP with the spin period  $P = 3.68$  ms and a  
 302 spin-down rate  $\dot{P} = 2.1 \times 10^{-20} \text{ s s}^{-1}$  (see Ransom et al. 2010), one can calculate the correspond-  
 303 ing spin-down luminosity as  $L_{\text{sd}} = 4\pi^2 I \dot{P} P^{-3} \simeq 2 \times 10^{34} \text{ erg s}^{-1}$ , and the magnetic field in-  
 304 tensity at the light cylinder (radius,  $R = cP/2\pi$ ) as  $B_{\text{lc}} \simeq 4\pi^2(3I\dot{P}/2c^3P^5)^{1/2} \simeq 5 \times 10^4 \text{ G}$ ,  
 305 where  $I = 10^{45} \text{ g cm}^2$  is the star’s moment of inertia. Meanwhile, for the claimed distance  
 306  $d \simeq 0.4 \text{ kpc}$  (Ransom et al. 2010), the observed  $\gamma$ -ray luminosity of PSR J1231–1411 leads as  
 307  $L_\gamma \simeq 2 \times 10^{33} \text{ erg s}^{-1}$ , its non-thermal X-ray luminosity is  $L_X \simeq 10^{30} \text{ erg s}^{-1}$ , and the total X-  
 308 ray luminosity  $L_{X/\text{tot}} \sim 3 \times 10^{30} \text{ erg s}^{-1}$ . These values are then consistent with the millisec-  
 309 ond pulsar scenario – outer-magnetosphere models in particular – in a framework of which one  
 310 should expect  $L_\gamma \sim 0.1 L_{\text{sd}}$  (Abdo et al. 2009d) and  $L_X \sim 10^{-3} L_{\text{sd}}$  (Becker & Truemper 1997;  
 311 Gaensler & Slane 2006; Zhang et al. 2007), with relatively large dispersion, however. Interest-  
 312 ingly, the synchrotron X-ray luminosity produced close to the light cylinder within the expected  
 313 magnetic field  $B_{\text{lc}}$  and a fraction (say, 10%) of the volume  $V \sim R^3$ , would then be close to  
 314 the observed non-thermal X-ray luminosity assuming rough energy equipartition between ultra-  
 315 relativistic electrons and the magnetic field.

316 In the case of 1FGL J1311.7–3429, two potential X-ray counterparts have been discovered  
 317 in our *Suzaku* observations. The association of this *Fermi* object with the northern source src A  
 318 is more likely, since the southern X-ray spot src B is located only marginally within the 95%  
 319 *Fermi*/LAT error circle of the  $\gamma$ -ray emitter. Yet the classification of 1FGL J1311.7–3429/src A,  
 320 for which the broad-band spectrum (including radio and optical upper limits) is shown in Fig-

321 ure 14, remains vague. Currently, no radio or  $\gamma$ -ray pulsations have been found at the position of  
 322 1FGL J1311.7–3429, and this favors an extragalactic origin of the detected high-energy emission.  
 323 And indeed, the flat X-ray continuum ( $\Gamma \simeq 1.4$ ) and the  $\gamma$ -ray-to-X-ray energy flux ratio  $\gtrsim 100$   
 324 (with  $S_{0.1-10\text{ GeV}} \simeq 6.4 \times 10^{-11} \text{ erg cm}^{-2} \text{ s}^{-1}$  as given in the 1FGL catalog) would be consistent  
 325 with the characteristics of luminous blazars of the FSRQ type (e.g., Sikora et al. 2009). On the  
 326 other hand, however, the radio upper limit indicating the GHz energy flux  $\simeq 10^{-5}$  times smaller  
 327 than the GeV energy flux, invalidates the blazar nature of 1FGL J1311.7–3429. That is because  
 328 all active galaxies established till now as  $\gamma$ -ray emitters are characterized by relatively strong,  
 329 Doppler-boosted radio emission. In particular, radio energy fluxes of bona fide blazars included  
 330 in 0FGL are, for a given *Fermi*/LAT photon flux of  $\sim 10^{-7} \text{ photons cm}^{-2} \text{ s}^{-1}$ , at least an order  
 331 of magnitude higher than the energy flux implied by the NVSS upper limits for src A (see, e.g.,  
 332 Kovalev et al. 2009). In addition, a very prominent 10 ks-long X-ray flare detected from src A, to-  
 333 gether with the steady GeV flux of 1FGL J1311.7–3429, would not match easily a typical behavior  
 334 of FSRQs: this class of blazars is known for displaying dramatic variability at GeV photon ener-  
 335 gies, but only modest variations in the X-ray band. Therefore, the nature of the analyzed *Fermi*  
 336 source and its newly discovered *Suzaku* counterpart remains an open question.

337 Within the error circle of 1FGL J1333.2+5056, our *Suzaku*/XIS observations revealed the  
 338 presence of several weak X-ray flux maxima with possibly diverse spectral properties (as indi-  
 339 cated by the spectral analysis hampered by the limited photon statistics). One of the detected  
 340 X-ray sources (src D) coincides with the high-redshift blazar CLASS J1333+5056 ( $z = 1.362$ ).  
 341 The broad-band spectral energy distribution of 1FGL J1333.2+5056/CLASS J1333+5056/src D is  
 342 presented in Figure 15, including the LAT  $\gamma$ -ray, *Suzaku* X-ray, archival radio, and newly ana-  
 343 lyzed *Swift*/UVOT data for the blazar. The constructed SED reveals two distinct radiative compo-  
 344 nents, consisting of a low-energy synchrotron bump and an (energetically dominant) high-energy  
 345 inverse-Compton continuum, reminiscent of typical broad-band spectra for blazars of the FSRQ  
 346 type (Ghisellini et al. 1998). Note that the X-ray-to- $\gamma$ -ray flux ratio  $\simeq 10^3$  implied by Figure 15,  
 347 as well as the relatively large radio flux, would be both in agreement with the blazar identification  
 348 of 1FGL J1333.2+5056. In addition, we note that the discussed *Fermi* object is the most variable  
 349 in  $\gamma$ -rays out of all four *Fermi* targets studied in this paper, with the variability index of 38 (which  
 350 indicates a  $< 1\%$  probability of a steady flux; see Abdo et al. 2010c). The additional support for  
 351 the blazar association is offered by the fact that the  $\gamma$ -ray continuum of 1FGL J1333.2+5056 is the  
 352 steepest among the four *Fermi* objects observed by us, with the photon index  $\simeq 2.5 \pm 0.1$ , which  
 353 is compatible with the mean  $\gamma$ -ray photon index of the FSRQ population reported in the 1FGL,  
 354 namely  $2.47 \pm 0.19$  (Abdo et al. 2010f).

355 Finally, in the case of 1FGL J2017.3+0603, the MSP PSR J2017+0603 was newly discov-  
 356 ered by the Nancay Radio Telescope (Cognard et al. 2010), and the association between the ra-  
 357 dio and  $\gamma$ -ray sources was confirmed by the pulse detection with the same period in the LAT

358 data. Interestingly, in our *Suzaku*/XIS exposure we have only detected the high-redshift blazar  
 359 ( $z = 1.743$ ) CLASS J2017+0603, but not the pulsar. The same is true for the *Swift*/UVOT ob-  
 360 servation (Cognard et al. 2010), which resulted in analogous flux and upper limit measurements  
 361 in the optical for the blazar and pulsar, respectively. The constructed radio to X-ray SEDs for the  
 362 pulsar and blazar systems are shown in Figure 16 together with the LAT spectrum. Regarding the  
 363 pulsar, Cognard et al. (2010) discovered that PSR J2017+0603 is located at a distance  $d \simeq 1.6$  kpc,  
 364 and as such is characterized by the spin-down luminosity  $L_{\text{sd}} \sim 1.34 \times 10^{34}$  erg s $^{-1}$ . The X-ray  
 365 (2 – 8 keV) luminosity derived from the *Suzaku*/XIS upper limit for this pulsar,  $L_X < 8.0 \times$   
 366  $10^{30}$  erg s $^{-1}$ , is then consistent with the expected “pulsar-like” luminosity ratio  $L_X/L_{\text{sd}} \sim 10^{-3}$ .  
 367 The overall curved  $\gamma$ -ray spectrum of 1FGL J2017.3+0603, characterized by the small photon  
 368 index  $\simeq 1.88 \pm 0.05$ , supports the pulsar association. On the other hand, the relatively large  
 369 radio flux of CLASS J2017+0603, together with the X-ray-to- $\gamma$ -ray flux ratio  $\simeq 300$  for the  
 370 1FGL J2017.3+0603/CLASS J2017+0603 system, are in some level of agreement with the blazar  
 371 interpretation. The  $\gamma$ -ray photon index of 1FGL J2017.3+0603 is however rather flat for a FSRQ  
 372 and represents a  $\sim 3\sigma$  deviation from the distribution observed for FSRQs (mean= 2.47,  $\sigma = 0.19$ ;  
 373 see Abdo et al. 2010f) thus making the association with the FSRQ less likely. Although the de-  
 374 tected pulsations in radio and  $\gamma$ -rays is key to the identification of the  $\gamma$ -ray source with a pulsar,  
 375 there may be some contaminating flux from the blazar. Indeed, the chance probability of finding a  
 376 CLASS-like background blazar in the Fermi error circle of this source is  $\sim 0.003\%$ . Considering  
 377 over 1400 sources in the 1FGL catalog, such ‘mixed’ cases could be expected.

## 378 4.2. Implications

379 What class of astrophysical objects can be in general associated with the unidentified high  
 380 Galactic latitude  $\gamma$ -ray sources? It was noted, for example, that compact and relatively nearby  
 381 molecular clouds exist at  $|b| > 10^\circ$ , and these should emit  $\gamma$ -rays at least at some level. Torres et al.  
 382 (2005) argued, however, that the expected GeV emission of such clouds is too low to account for  
 383 the observed fluxes of unidentified EGRET sources, and the same applies to the bright unidentified  
 384 *Fermi*/LAT objects. Another classes of possible counterparts proposed were radio-quiet pulsars and  
 385 isolated neutron stars (e.g., Yadigaroglu & Romani 1995), and this idea has indeed been validated  
 386 by the subsequent multi-frequency studies, as discussion in § 1. We note in this context that the  
 387 Galactic origin of high-latitude  $\gamma$ -ray emitters is especially probable for the objects located at  $10^\circ \leq$   
 388  $|b| \leq 30^\circ$  within the Gould Belt ( $\sim 0.3$  kpc from the Earth), which constitutes an aggregation of  
 389 massive late-type stars, molecular clouds, and supernova remnants (Grenier et al. 2000).

390 A probably more challenging population of  $\gamma$ -ray emitters is represented by the isotropic com-  
 391 ponent of the unidentified EGRET objects, consisting of about 60 sources (about one third of which

392 with the Galactic latitudes  $|b| > 45^\circ$ , including several non/weakly-variable during the EGRET ob-  
 393 servations; Özel & Thompson 1996; Gehrels et al. 2000). For those sources, Totani & Kitayama  
 394 (2000) have for example suggested associations with large-scale shocks produced during the struc-  
 395 ture formation in the intergalactic medium (see also Waxman & Loeb 2000). Totani & Kitayama  
 396 explored the connection between steady GeV objects located off the Galactic plane, and labeled  
 397 in the 3EG catalog as “possibly extended,” with dynamically forming clusters of galaxies (and  
 398 not single virialized cluster systems; see Kawasaki & Totani 2002). However, the non-variable  
 399 nature of the  $\gamma$ -ray emission of several of the considered objects was questioned (see Reimer et al.  
 400 2003, and references therein), and the high efficiency of the particle acceleration at the structure  
 401 formation shocks required by the model was also noted (e.g., Keshet et al. 2003).

402 Radio galaxies are prime candidates for the unidentified high Galactic latitude EGRET sources,  
 403 especially since the only confirmed non-blazar AGN detected previously at GeV photon energies  
 404 was the nearby radio galaxy Centaurus A (Steinle et al. 1998; Sreekumar et al. 1999). Yet no other  
 405 radio galaxy has been firmly detected by EGRET at the significance level high enough ( $\geq 4\sigma$ ) to  
 406 be included in the 3rd EGRET catalog (Hartman et al. 1999). Moreover, Cillis et al. (2004), who  
 407 applied a stacking analysis of the EGRET data for a sample of the brightest and/or the closest radio  
 408 and Seyfert galaxies, showed that ‘no detection significance greater than  $2\sigma$  has been found for any  
 409 subclass, sorting parameter, or number of objects co-added.’ Nevertheless, Mukherjee et al. (2002)  
 410 argued that the most likely counterpart to the unidentified EGRET source 3EG J1621+8203 is the  
 411 bright radio galaxy NGC 6251. A marginal detection of 3C111 with EGRET has also been reported  
 412 (Hartman, Kadler & Tueller 2008). We also note that Combi et al. (2003) reported the discovery  
 413 of a new radio galaxy within the location error circle of the unidentified  $\gamma$ -ray source 3EG J1735–  
 414 1500. The identification of 3EG J1735–1500 was however controversial, due to the presence of an  
 415 another likely (blazar-type) candidate within the EGRET error contours (Sowards-Emmerd et al.  
 416 2004). The most recent analysis based on the 15 months of *Fermi*/LAT data resulted in the detection  
 417 of 11 non-blazar-type AGN (all radio galaxies), including the aforementioned cases of NGC 6251  
 418 and 3C111 (Abdo et al. 2010g). The idea that some fraction of unidentified  $\gamma$ -ray emitters may be  
 419 associated with faint radio galaxies is therefore validated, although this should rather apply to only  
 420 dimmer *Fermi* objects, and not to the population of exceptionally bright  $\gamma$ -ray sources detected  
 421 already by EGRET.

422 The *Suzaku*/XIS studies of four bright *Fermi*/LAT objects reported here provide an impor-  
 423 tant contribution to the debate regarding the nature of unidentified  $\gamma$ -ray emitters located at high  
 424 Galactic latitudes. In particular, our observations support the idea that a significant fraction of  
 425 such objects may be associated with old ( $\gtrsim$  Gyr) MSPs present within the Galactic halo and the  
 426 Earth’s neighborhood (such as 1FGL J1231.1–1410 and 1FGL J2017.3+0603). Yet not all of the  
 427 unidentified *Fermi* objects are related to the pulsar phenomenon. Instead, some of those may  
 428 be hosted by active galaxies, most likely by the luminous and high-redshift blazars of the FSRQ

429 type (1FGL J1333.2+5056 is as good blazar candidate, for example). However, there still remain  
 430 unidentified sources, (e.g., 1FGL J1311.7–3429), for which neither blazar nor pulsar scenarios  
 431 seem to apply. For these, ultra-deep multi-wavelength studies are probably needed to unravel their  
 432 physical nature.

## 433 5. Summary

434 In this paper we reported on the results of deep X-ray follow-up observations of four uniden-  
 435 tified  $\gamma$ -ray sources detected by the *Fermi*/LAT instrument at high Galactic latitudes ( $|b| > 10^\circ$ )  
 436 using the X-ray Imaging Spectrometers onboard *Suzaku* satellite. All of the studied objects have  
 437 been detected at high significance ( $> 10\sigma$ ) during the first 3-months of the *Fermi*/LAT operation.  
 438 For some of them, possible associations with pulsars and blazar have been recently discussed, and  
 439 our observations provide an important contribution to this debate. In particular, an X-ray point  
 440 source was newly found within 95% error circle of 1FGL J1231.1–1410. The X-ray spectrum of  
 441 the discovered *Suzaku* counterpart of 1FGL J1231.1–1410 is well fitted by a blackbody emission  
 442 with a temperature of  $kT \simeq 0.16$  keV plus an additional power-law component with a differential  
 443 photon index  $\Gamma \simeq 1.8$ . This supports the recently claimed identification of this source with a MSP  
 444 PSR J1231–1411. For the remaining three *Fermi* objects, the performed X-ray observations are  
 445 less conclusive. In the case of 1FGL J1311.7–3429, two possibly associated X-ray point sources  
 446 were newly found. Even though the 0.4 – 10 keV spectral and variability properties for those  
 447 could be robustly accessed, the physical nature of the X-ray emitters and their relations with the  
 448  $\gamma$ -ray source remain unidentified. Similarly, we found several weak X-ray sources in the field of  
 449 1FGL J1333.2+5056, one coinciding with the high-redshift blazar CLASS J1333+5057. We ar-  
 450 gue that the available data are consistent with the physical association between these two objects,  
 451 even though we were not able to identify robustly the *Suzaku* counterpart of  $\gamma$ -ray emitter due to a  
 452 large positional uncertainty of 1FGL J1333.2+5056. Finally, we found an X-ray point source in the  
 453 vicinity of 1FGL J2017.3+0603. This *Fermi* object was recently suggested to be associated with  
 454 a newly discovered MSP PSR J2017+0603 because of the detection of radio and  $\gamma$ -ray pulsations.  
 455 However, we did not detect the X-ray counterpart of the pulsar, but instead of the high-redshift  
 456 blazar CLASS J2017+0603 located within the error circle of 1FGL J2017.3+0603. Still, the result-  
 457 ing upper limits for the X-ray emission do not invalidate the pulsar association.

458 Ł.S. is grateful for the support from Polish MNiSW through the grant N-N203-380336.

## REFERENCES

459

460 Abdo, A. A., et al. (*Fermi*-LAT Collaboration) 2009a, *ApJ*, 700, 597

461 Abdo, A. A., et al. (*Fermi*-LAT Collaboration) 2009b, *ApJ*, 700, 1059

462 Abdo, A. A., et al. (*Fermi*-LAT Collaboration) 2009c, *ApJS*, 183, 46

463 Abdo, A. A., et al. (*Fermi*-LAT Collaboration) 2009d, *Science*, 325, 840

464 Abdo, A. A., et al. (*Fermi*-LAT Collaboration) 2010a, *ApJ*, 712, 1209

465 Abdo, A. A., et al. (*Fermi*-LAT Collaboration) 2010b, *ApJ*, 712, 957

466 Abdo, A. A., et al. (*Fermi*-LAT Collaboration) 2010c, *ApJS*, 188, 405

467 Abdo, A. A., et al. (*Fermi*-LAT Collaboration) 2010d, *ApJ*, 715, 429

468 Abdo, A. A., et al. (*Fermi*-LAT Collaboration) 2010e, *ApJS*, 187, 460

469 Abdo, A. A., et al. (*Fermi*-LAT Collaboration) 2010f, *ApJ*, 720, 435

470 Abdo, A. A., et al. (*Fermi*-LAT Collaboration) 2010f, *ApJ*, 720, 912

471 Adelman-McCarthy, J. K., et al. 2008, *ApJS*, 175, 297

472 Atwood, W. B., et al. 2009, *ApJ*, 697, 1071

473 Becker, W., & Truemper, J. 1997, *A&A*, 326, 682

474 Casandjian, J.-M., & Grenier, I. A. 2008, *A&A*, 489, 849

475 Cillis, A. N., Hartman, R. C., & Bertsch, D. L. 2004, *ApJ*, 601, 142

476 Combi, J. A., et al. 2003, *ApJ*, 588, 731

477 Cognard, I., et al. 2010, submitted

478 Condon, J. J., et al. 1998, *AJ*, 115, 1693

479 Day, C., et al. 1998, *The ASCA Data Reduction Guide*, Tech. Rep., (Greenbelt: NASA GSFC),  
480 v.2.0

481 Dickey, J. M., & Lockman, F. J. 1990, *ARA&A*, 28, 215

482 Gaensler, B. M., & Slane, P. O. 2006, *ARA&A*, 44, 17



- 483 Gehrels, N., & Michelson, P. 1999, *Astropart. Phys.*, 11, 277
- 484 Gehrels, N., et al. 2000, *Nature*, 404, 363
- 485 Ghisellini, G., et al. 1998, *MNRAS*, 301, 451
- 486 Gregory, P. C., et al. 1996, *ApJS*, 103, 427
- 487 Grenier, I. A. 2000, *A&A*, 364, 93
- 488 Halpern, J. P., et al. 2001, *ApJ*, 551, 1016
- 489 Halpern, J. P. et al. 2002, *ApJ*, 573, L41
- 490 Halpern, J. P. et al. 2008, *ApJ*, 688, L33
- 491 Hartman, R. C., et al. 1999, *ApJS*, 123, 79
- 492 Hartman, R. C., Kadler, M., & Tueller, J. 2008, *ApJ*, 688, 852
- 493 Ishisaki, Y., et al. 2007, *PASJ*, 59, S113
- 494 Kawasaki, W., & Totani, T. 2002, *ApJ*, 576, 679
- 495 Keshet, U., et al. 2003, *ApJ*, 585, 128
- 496 Kokubun, M., et al. 2007, *PASJ*, 59, S53
- 497 Kovalev, Y. Y., et al. 2009, *ApJ*, 696, 17
- 498 Koyama, K., et al. 2007, *PASJ*, 59, S23
- 499 Myers, S. T. et al., 2003, *MNRAS*, 341, 1
- 500 Mirabal, N., et al. 2000, *ApJ*, 541, 180
- 501 Mitsuda, K., et al., 2007, *PASJ*, 59, 1
- 502 Morrison, R., & McCammon, D. 1983, *ApJ*, 270, 119
- 503 Mukherjee, R., et al. 2000, *ApJ*, 542, 740
- 504 Mukherjee, R., et al. 2002, *ApJ*, 574, 693
- 505 Mukherjee, R., & Halpern, J. 2004, *Cosmic Gamma-Ray Sources*, Eds. K.S. Cheng &  
506 G.E. Romero, 304, 311

- 507 Nolan, P. L., et al. 2003, ApJ, 597, 615
- 508 Özel, M. E., & Thompson, D. J. 1996, ApJ, 463, 105
- 509 Ransom, S. M., et al., 2010, ApJ, 727, L16
- 510 Reimer, O., 2001, in proc. *‘The Nature of Unidentified Galactic High-Energy Gamma-Ray*  
511 *Sources’*, eds. A. Carraminana, O. Reimer, & D. J. Thompson (Kluwer Academic Pub-  
512 *lishers: Dordrecht*), 17
- 513 Reimer, O., et al. 2001, MNRAS, 324, 772
- 514 Reimer, O., et al. 2003, ApJ, 588, 155
- 515 Shaw, M. S., et al. 2009, ApJ, 704, 477
- 516 Sikora, M., et al. 2009, ApJ, 704, 38
- 517 Sowards-Emmerd, D., et al. 2003, ApJ, 590, 109
- 518 Sowards-Emmerd, D., Romani, R. W., & Michelson, P. F. 2004, ApJ, 609, 564
- 519 Sreekumar, P., et al. 1999, APh, 11, 221
- 520 Steinle, H., et al., 1998, A&A, 330, 97
- 521 Takahashi, T., et al. 2007, PASJ, 59S, 35
- 522 Tavani, M., et al. 2009, A&A, 502, 995
- 523 Tawa, N., et al. 2008, PASJ, 60S, 11
- 524 Thompson, D. J., et al. 1999, ApJ, 516, 297
- 525 Torres, D. F., Dame, T. M., & Digel, S. W. 2005, ApJ, 621, L29
- 526 Totani, T., & Kitayama, T. 2000, ApJ, 545, 572
- 527 Waxman, E & Loeb, E. 2000, ApJ, 545, L11
- 528 Yadigaroglu, I. A., & Romani, R. W. 1995, ApJ, 449, 211
- 529 Zhang, L., et al. 2007, ApJ, 666, 1165

Table 1: EGRET and *Fermi*/LAT entries for the analyzed objects

Name	RA [deg]	DEC [deg]	$l$ [deg]	$b$ [deg]	$F_{0.1-20\text{ GeV}}$ [ $10^{-8}\text{ ph cm}^{-2}\text{ s}^{-1}$ ]	$r_{95\%}$ [deg]
1FGLJ1231.1–1410 <sup>†</sup>	187.80	–14.17	295.53	+48.41	14.9±0.7	0.03
3EGJ1234–1318 (EGRJ1231–1412)	188.19	–16.30	296.43	+49.34	21.6±5.3	0.76
1FGLJ1311.7–3429 <sup>§</sup>	197.95	–34.49	307.69	+28.19	11.7±1.1	0.04
3EGJ1314–3431 (EGRJ1314–3417)	198.51	–34.52	308.21	+28.12	18.7±3.1	0.56
1FGLJ1333.2+5056 <sup>§</sup>	203.30	+50.94	107.32	+64.90	4.5±1.0	0.15
3EGJ1337+5029 (EGRJ1338+5102)	204.39	+50.49	105.40	+65.04	9.2±2.6	0.72
1FGLJ2017.3+0603 <sup>‡</sup>	304.34	+6.05	48.62	–16.02	4.5±0.5	0.04

<sup>†</sup> Data consistent with no variability between EGRET and *Fermi*/LAT observations.

<sup>§</sup> The  $\gamma$ -ray fluxes determined by EGRET and *Fermi*/LAT marginally consistent within  $2\sigma$  level.

<sup>‡</sup> Data consistent with no variability between EGRET and *Fermi*/LAT observations because of the EGRET detection limit  $\simeq 6 \times 10^{-8}\text{ ph cm}^{-2}\text{ s}^{-1}$ .

Table 2: *Suzaku*/XIS Observation Log

Name	OBS ID	Pointing Center*		Observation start (UT)	Effective exposure [ksec]
		RA [deg]	DEC [deg]		
1FGLJ1231.1–1410	804017010 <sup>†</sup>	187.8001	–14.1665	2009/07/08 22:53:48	23.8
	804017020 <sup>†</sup>	187.7993	–14.1672	2009/07/28 05:21:37	44.8
1FGLJ1311.7–3429	804018010	197.9603	–34.4918	2009/08/04 04:56:35	33.0
1FGLJ1333.2+5056	804019010	203.2955	51.0170	2009/06/01 10:13:15	39.1
1FGLJ2017.3+0603	804020010	304.3461	6.0496	2009/10/27 10:14:45	26.7

\* The pointing centers were the positions given in 0FGL catalog (Abdo et al. 2009c).

<sup>†</sup> The requested continuous 80 ks *Suzaku* exposure was interrupted by Target of Opportunity (ToO) observation of GRB 090708. For this reason the observation was divided into 30 ks and 50 ks segments before and after the ToO observation.

Table 3: Source detection results of *Suzaku* observation

Name		Position		Detection Significance	$r_{95\%}$
		RA [deg]	DEC [deg]	$\sigma$	[arcsec]
1FGL J1231.4–1410	—	187.790	–14.192	13.67	7.44
1FGL J1311.7–3429	src A	197.939	–34.508	15.52	17.44
	src B	197.942	–34.534	12.89	12.27
1FGL J1333.2+5056	src A	203.252	50.983	8.53	23.34
	src B	203.161	51.032	7.27	19.97
	src C	203.276	51.014	7.47	20.75
	src D	203.479	50.967	4.50	38.41
	src E	203.381	50.892	4.91	26.51
1FGL J2017.3+0603	—	304.310	6.052	14.44	4.73

Table 4: Fitting Parameters for 1FGL J1231.1–1410 in a framework of blackbody (BB) and power-law (PL) models

parameter	BB model value & error	BB+PL Model value & error
$N_H$ [ $10^{22}$ cm $^{-2}$ ]	0.0 (fixed)	0.0 (fixed)
$kT$ [keV]	$0.228 \pm 0.008$	$0.163^{+0.024}_{-0.026}$
norm. (BB)	$(1.42 \pm 0.14) \times 10^{-6}$	$(1.20^{+0.31}_{-0.37}) \times 10^{-6}$
$\Gamma$	—	$1.79^{+0.40}_{-0.17}$
norm. (PL)	—	$(1.94^{+1.14}_{-0.84}) \times 10^{-5}$
$\chi^2$	128.1	55.46
d.o.f.	34	32
reduced $\chi^2$	3.768	1.733
Flux (2 – 8 keV) [erg cm $^{-2}$ s $^{-1}$ ]	—	$(5.79^{+1.62}_{-1.52}) \times 10^{-14}$

Table 5: Blackbody (BB) and power-law (PL) components in the X-ray spectrum of 1FGL J1231.1–1410

	(i) Standard Background		(ii) Ring Background		(iii) Lockman Hole Background	
	BB	BB+PL	BB	BB+PL	BB	BB+PL
$\chi^2$	134.71	56.16	67.21	18.97	39.77	23.97
d.o.f.	34	32	30	28	38	36
F value	22.4		35.6		11.9	
Probability	$8.33 \times 10^{-7} \%$		$2.04 \times 10^{-6} \%$		$1.10 \times 10^{-2} \%$	

Table 6: Fitting Parameters for 1FGL J1311.7–3429 for power-law model

	src A	src B
parameter	value & error	value & error
$N_H$ [ $10^{20}$ cm $^{-2}$ ]	4.45 (fixed)	4.45 (fixed)
$\Gamma$	$1.38^{+0.13}_{-0.13}$	$1.34^{+0.16}_{-0.15}$
norm.	$(2.69^{+0.38}_{-0.37}) \times 10^{-5}$	$(2.08^{+0.34}_{-0.33}) \times 10^{-5}$
$\chi^2$	42.6	42.1
d.o.f.	38	38
reduced $\chi^2$	1.12	1.11
Flux (2 – 8 keV) [erg cm $^{-2}$ s $^{-1}$ ]	$(1.45^{+0.18}_{-0.18}) \times 10^{-13}$	$(1.20^{+0.18}_{-0.17}) \times 10^{-13}$



Table 7: Count rates and constant flux fits for X-ray sources within the error circle of 1FGL J1333.2+5056

Source	Average count rate & Error [ $10^{-3}$ ct s $^{-1}$ ]	$\chi^2$ /d.o.f.	Prob. [%]
src A	$5.47 \pm 0.51$	14.9/15	46.08
src B	$4.40 \pm 0.49$	22.4/15	9.73
src C	$4.37 \pm 0.48$	18.8/15	22.28
src D	$2.19 \pm 0.44$	20.5/15	15.25
src E	$1.70 \pm 0.44$	23.3/15	7.86

Table 8: Fitting Parameters for 1FGL J1333.2+5056 for power-law model

parameter	src A value & error	src B value & error	src C value & error	src D value & error	src E value & error
$N_H$ [ $10^{20}$ cm $^{-2}$ ]	1.09 (fixed)	1.09 (fixed)	1.09 (fixed)	1.09 (fixed)	1.09 (fixed)
$\Gamma$	2.35 $^{+0.35}_{-0.32}$	1.48 $^{+0.29}_{-0.27}$	1.51 $^{+0.31}_{-0.29}$	1.76 $^{+0.60}_{-0.52}$	2.50 $^{+0.69}_{-0.58}$
norm. [ $\times 10^{-5}$ ]	1.57 $^{+0.28}_{-0.28}$	1.07 $^{+0.27}_{-0.26}$	0.84 $^{+0.22}_{-0.22}$	0.77 $^{+0.31}_{-0.30}$	1.34 $^{+0.36}_{-0.37}$
$\chi^2$	13.0	7.33	18.3	12.7	11.4
d.o.f.	18	18	18	16	12
reduced $\chi^2$	0.720	0.407	1.02	0.796	0.949
Flux (2 – 8 keV) [ $\times 10^{-14}$ erg cm $^{-2}$ s $^{-1}$ ]	2.16 $^{+0.88}_{-0.75}$	4.98 $^{+1.46}_{-1.37}$	3.77 $^{+1.17}_{-1.11}$	2.41 $^{+1.55}_{-1.26}$	1.52 $^{+1.41}_{-0.94}$

Table 9: Fitting Parameters for 1FGL J2017.3+0603 for power-law model

parameter	value & error
$N_H$ [ $10^{22}$ cm $^{-2}$ ]	0.1309 (fixed)
$\Gamma$	$1.59^{+0.15}_{-0.15}$
norm.	$(5.03^{+0.68}_{-0.66}) \times 10^{-5}$
$\chi^2$	34.8
d.o.f.	38
reduced $\chi^2$	0.916
Flux (2 – 8 keV) [ erg cm $^{-2}$ s $^{-1}$ ]	$(1.99^{+0.28}_{-0.27}) \times 10^{-13}$

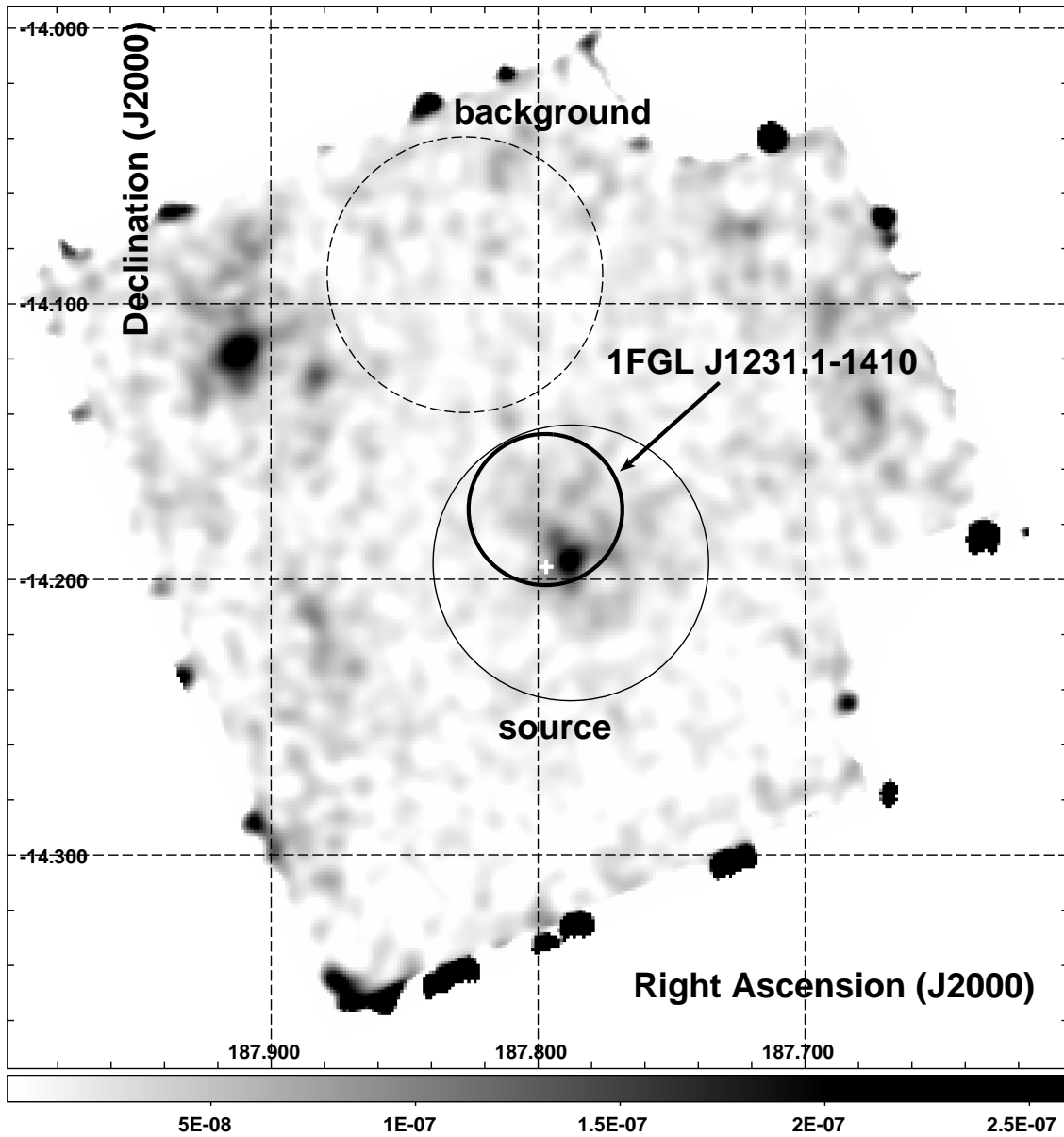


Fig. 1.— *Suzaku*/XIS FI (XIS0+3) image of 1FGLJ1231.1–1410 region in the 0.4 – 10 keV photon energy range. The image shows the relative excess of smoothed photon counts (arbitrary units indicated in the bottom bar) and is displayed with linear scaling. The areas enclosed by solid and dashed circles are source and background regions, respectively. Thick solid circle denotes 95% position error of 1FGL J1231.1–1410. White cross marks the position of radio MSP PSR J1231–1411 (Ransom et al. 2010).

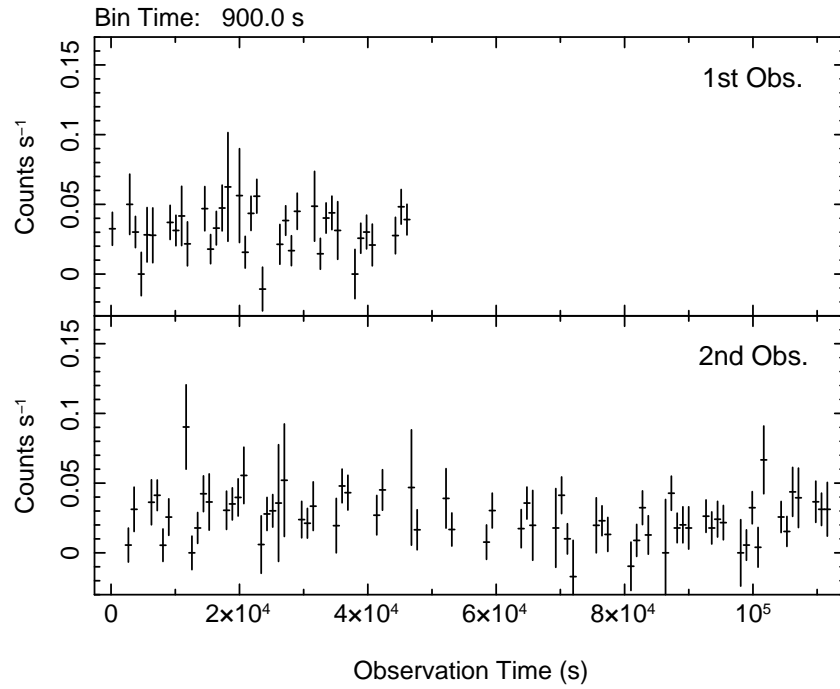


Fig. 2.— *Suzaku*/XIS light curves of the X-ray counterpart of 1FGL J1231.1–1410 during the 1st and the 2nd observations (upper and lower panels, respectively). Binning time applied is 900 s. The zero point of the upper and lower panels are MJD 55020.9971 and 55040.2343 (TDB: Barycentric Dynamical Time).

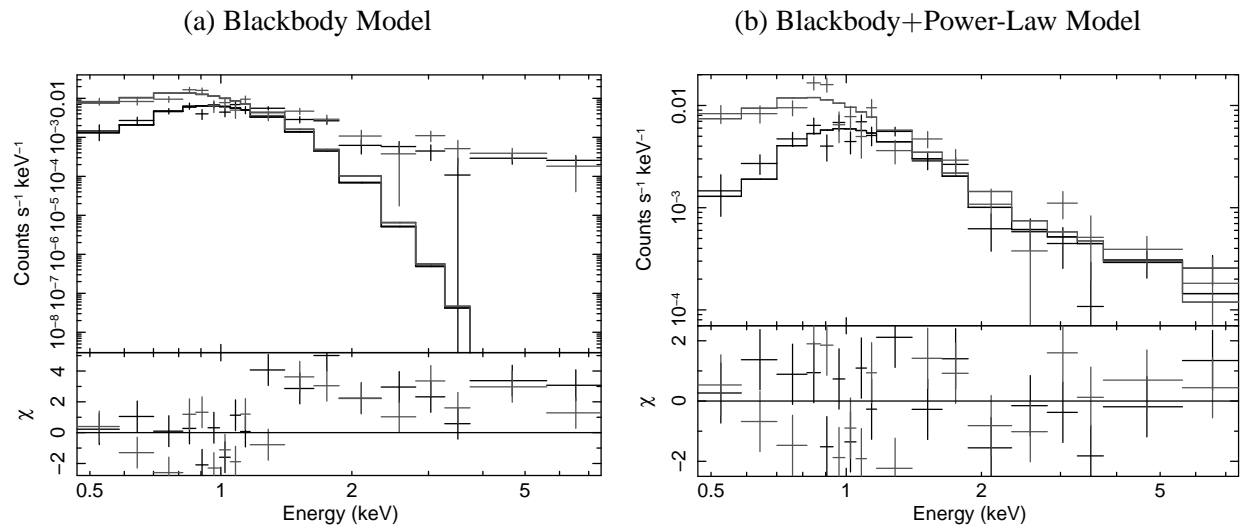


Fig. 3.— *Suzaku*/XIS spectra of the X-ray counterpart of 1FGLJ1231.1–1410 in the photon energy range 0.4 – 7.0 keV fitted with the blackbody model (a) and blackbody+power-law model (b). FI data are shown in black, and BI data in gray.

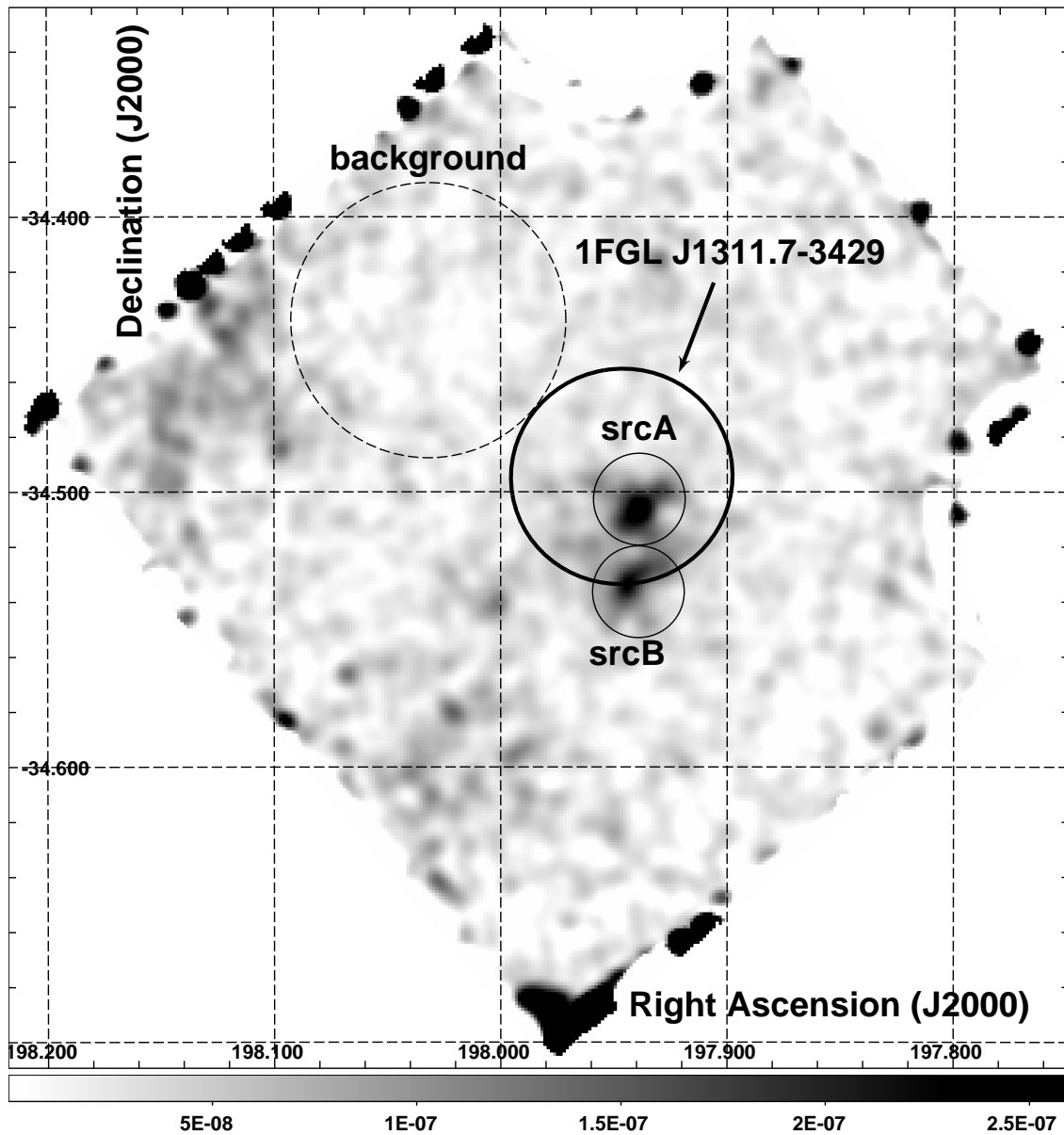


Fig. 4.— *Suzaku*/XIS FI (XIS0+3) image of 1FGL J1311.7–3429 region in the 0.4–10 keV photon energy range. The image shows the relative excess of smoothed photon counts (arbitrary units indicated in the bottom bar) and is displayed with linear scaling. The regions enclosed by solid and dashed circles are source and background regions, respectively. Thick solid circle denotes 95% position error of 1FGL J1311.7–3429. Within this error circle, two potential X-ray counterparts of the  $\gamma$ -ray source were found: src A and src B.

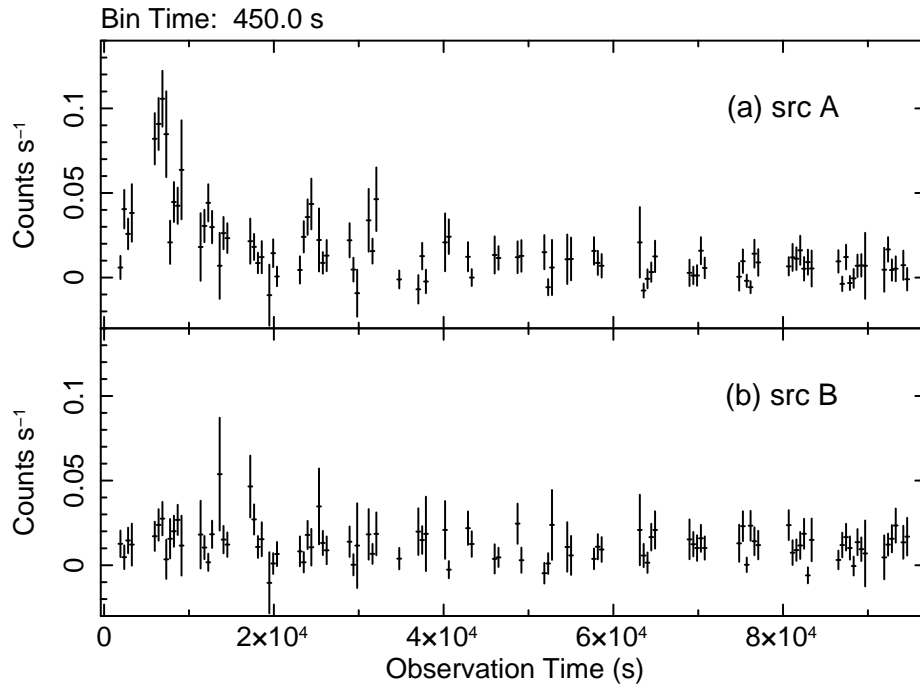


Fig. 5.— *Suzaku*/XIS light curves of two potential X-ray counterparts of 1FGL J1311.7–3429 with 450 s binning. The northern source src A (upper panel) showed highly significant X-ray flare in the first 20 ks of observation, during which the count rate increased by a factor of 10. The southern source src B (lower panel) was steady during the whole exposure. The zero point of src A and src B is MJD 55047.2280 (TDB).



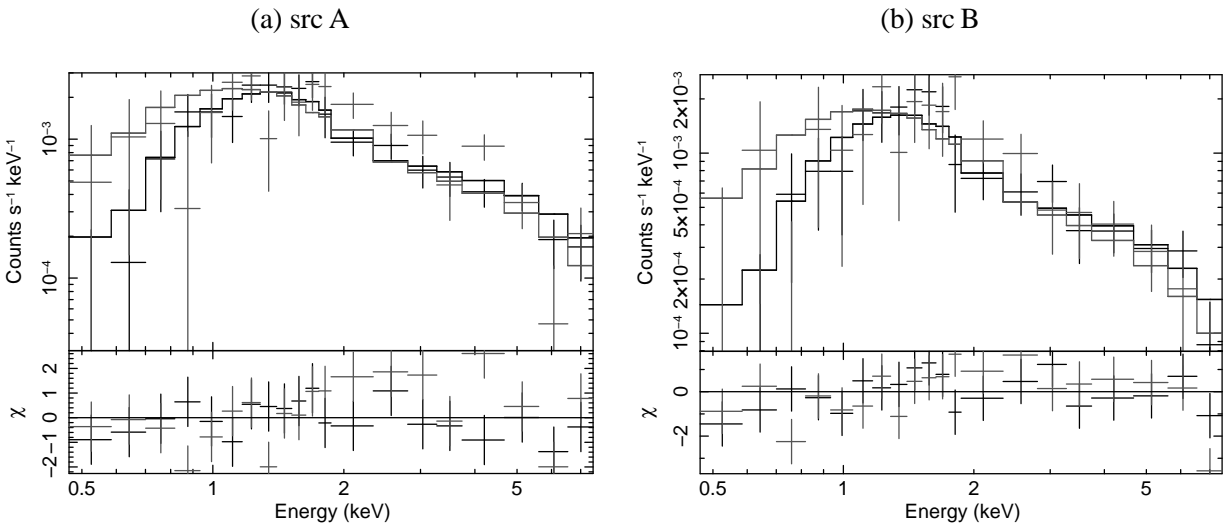


Fig. 6.— *Suzaku*/XIS Spectra of two possible X-ray counterparts of 1FGLJ1311.7–3429 in the photon energy range 0.4 – 8.0 keV fitted with the best fit power-law model. FI data are represented in black, and BI data in gray.

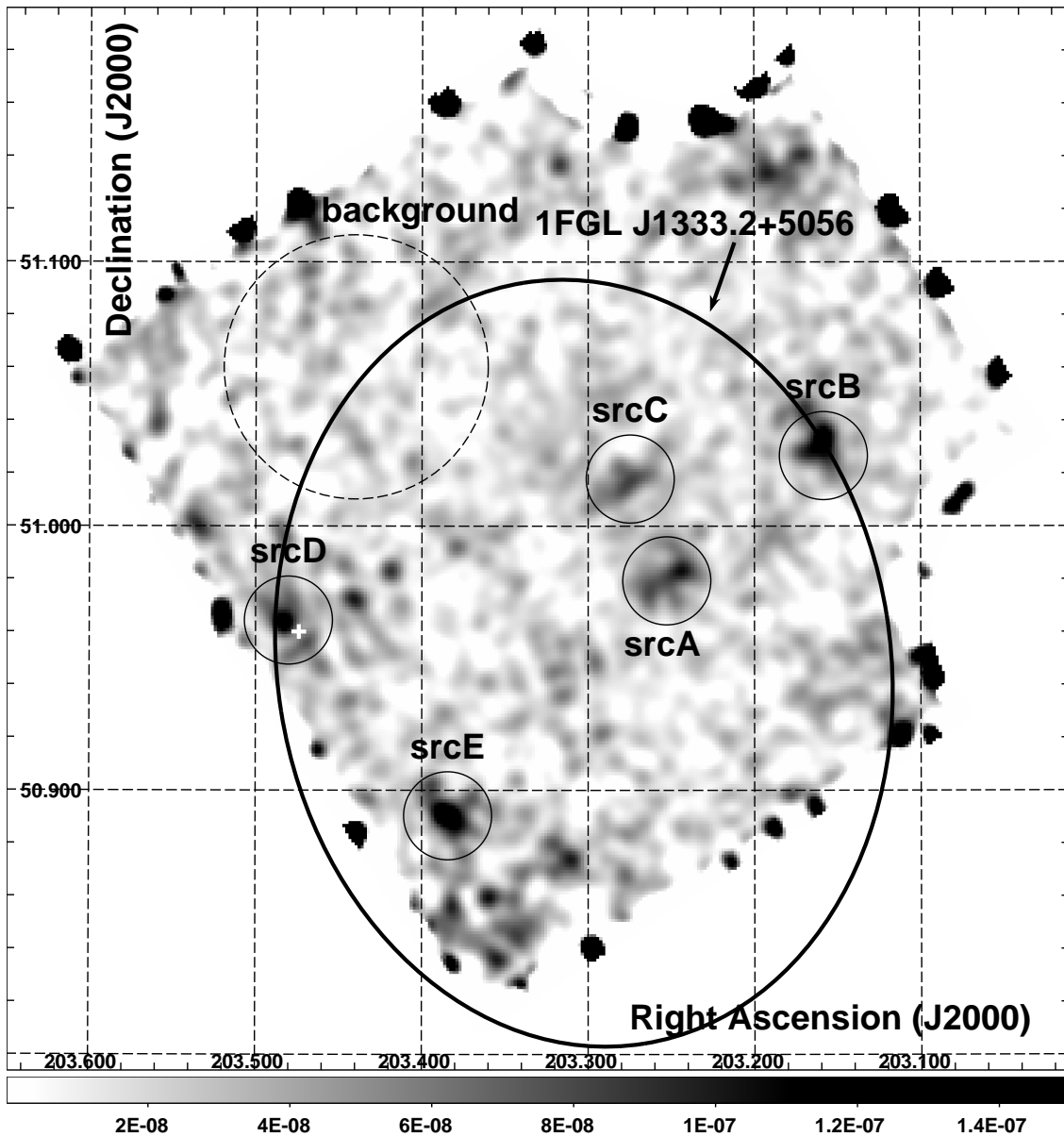


Fig. 7.— *Suzaku*/XIS FI (XIS0+3) image of the 1FGL J1333.2+5056 region in the 0.4 – 10 keV photon energy range. The image shows the relative excess of smoothed photon counts (arbitrary units indicated in the bottom bar) and is displayed with linear scaling. The regions enclosed by solid and dashed circles are source and background regions, respectively. Thick solid ellipsis denotes 95% position error of 1FGL J1333.2+5056. Within this error circle, several potential X-ray counterparts of the  $\gamma$ -ray object were found. White cross marks the position of active galaxy CLASS J1333+5057.

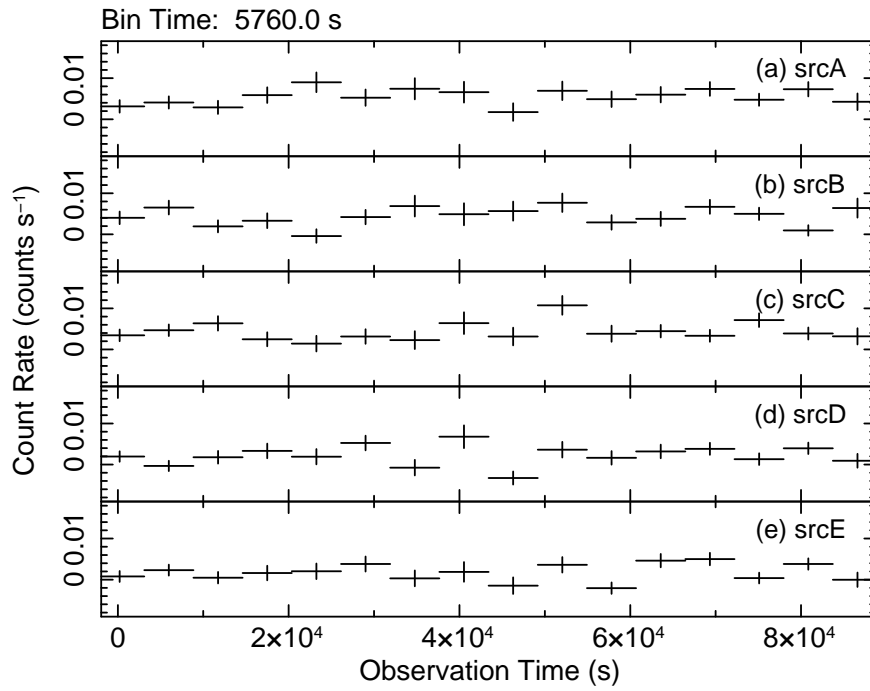


Fig. 8.— *Suzaku*/XIS light curves of potential X-ray counterparts of 1FGL J1333.2+5056 with the applied time binning of 5760 s. The zero point of time is MJD 54983.4274 (TDB).

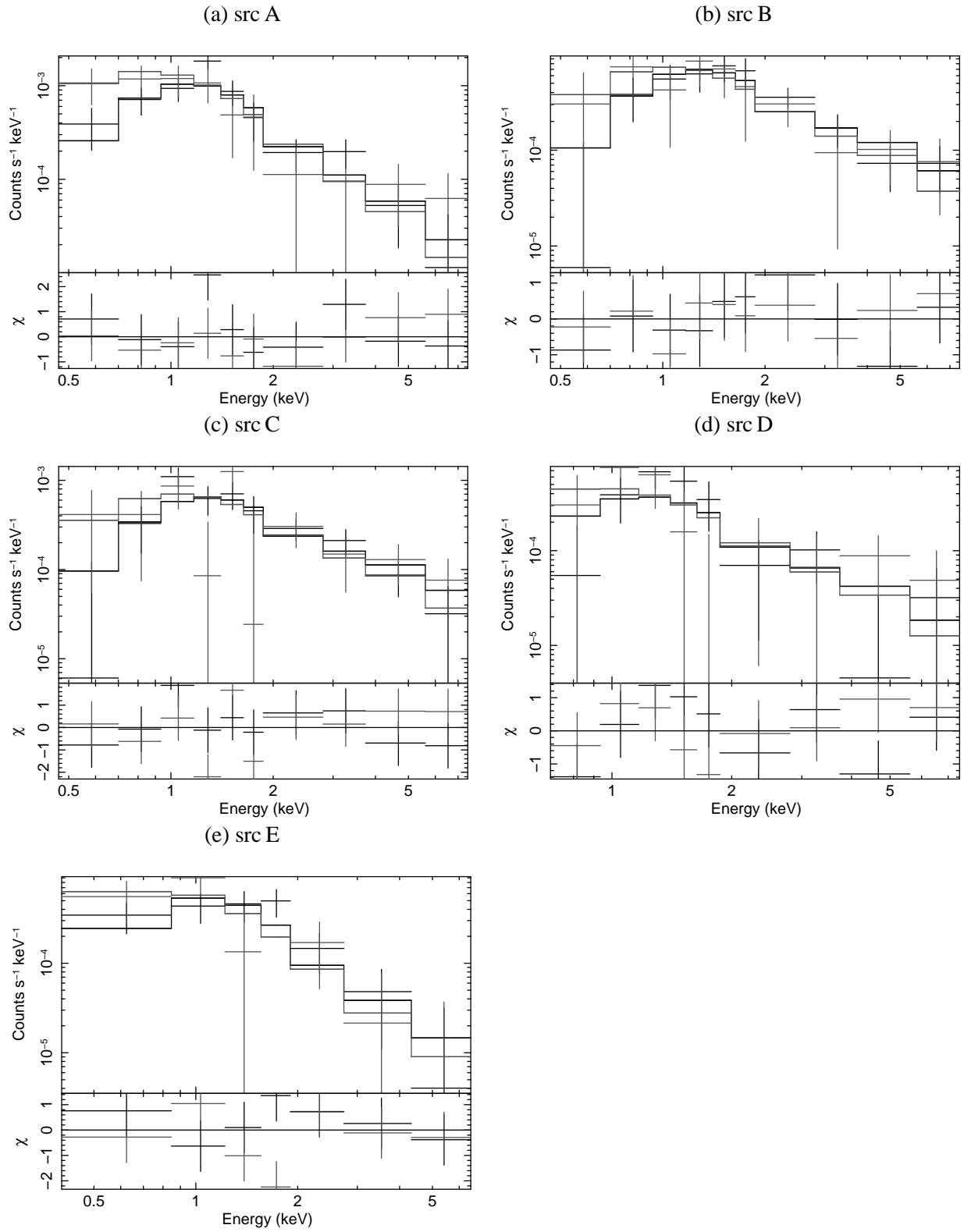


Fig. 9.— *Suzaku*/XIS spectra of the selected possible X-ray counterparts of 1FGL J1333.2+5056 fitted with a power-law model. FI data are represented in black, and BI data in gray.

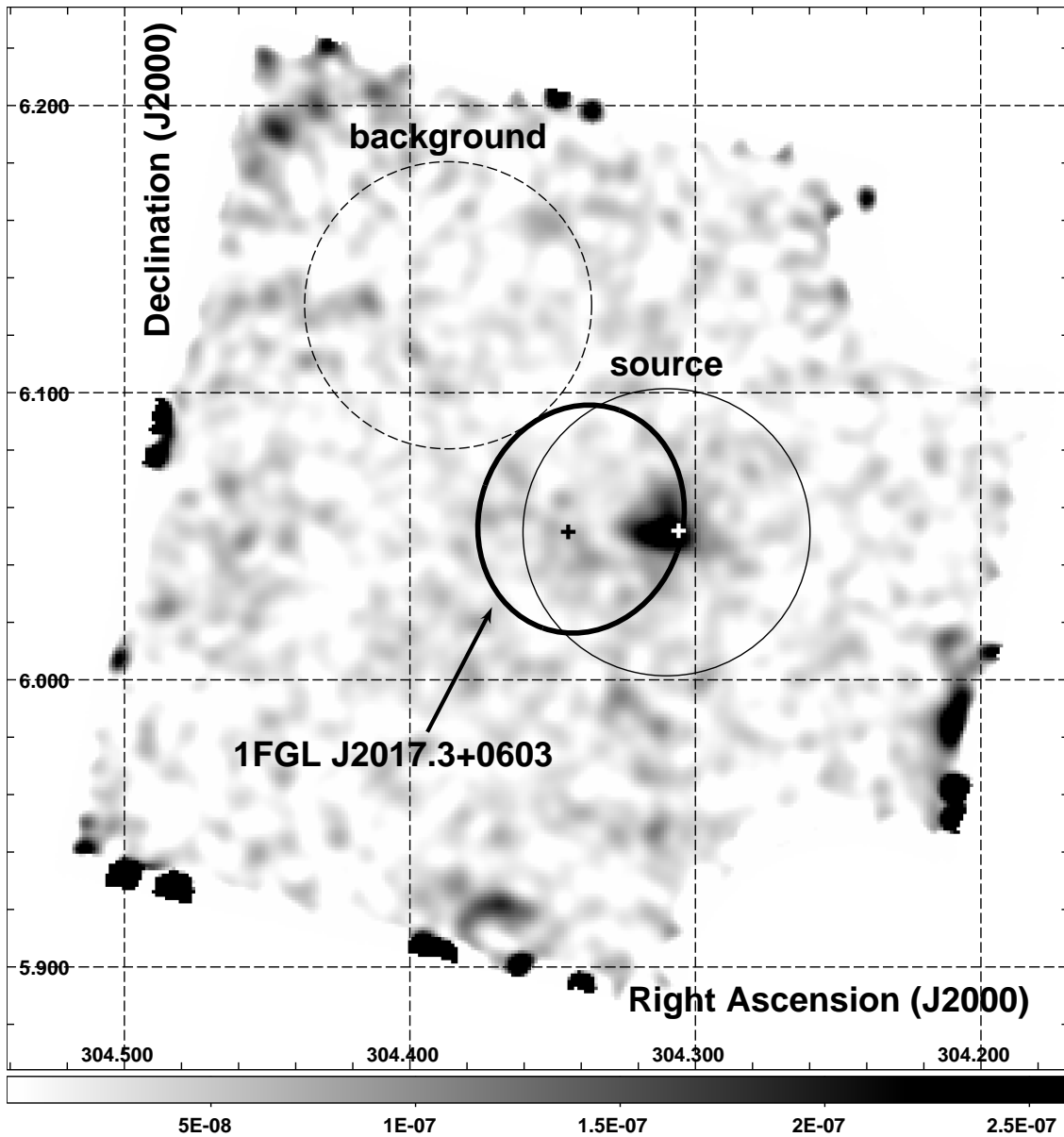


Fig. 10.— *Suzaku*/XIS FI (XIS0+3) image of the 1FGL J2017.3+0603 region in the 0.4 – 10 keV photon energy range. The image shows the relative excess of smoothed photon counts (arbitrary units indicated in the bottom bar) and is displayed with linear scaling. The regions enclosed by solid and dashed circles are source and background regions, respectively. Thick solid circle denotes 95% position error of 1FGL J2017.3+0603. One X-ray point source was found within this error circle. White cross mark denotes the position of the blazar CLASS J2017+0603. Black cross mark denotes the position of the radio MSP PSR J2017+0603 (Cognard et al. 2010).

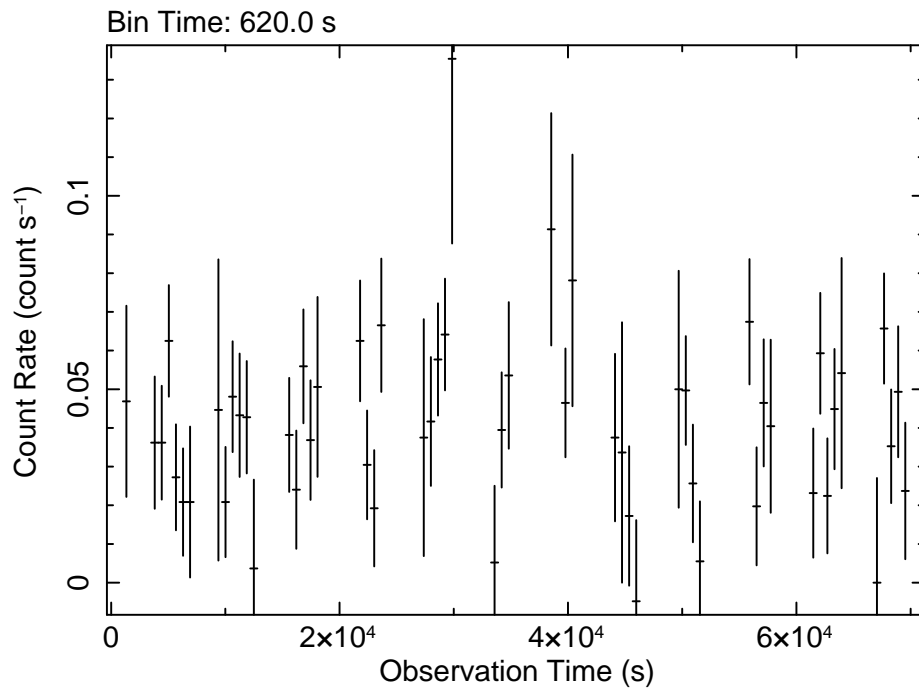


Fig. 11.— *Suzaku*/XIS light curve of an X-ray point source within the error circle of 1FGLJ2017.3+0603 with the applied 620 s time binning. The zero point of time is MJD 55131.4285 (TDB).

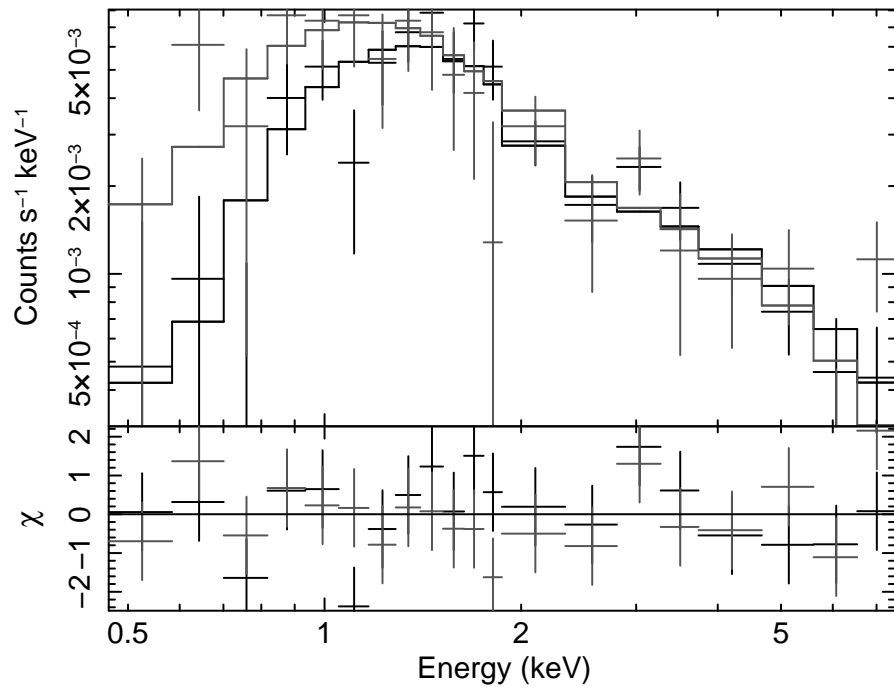


Fig. 12.— *Suzaku*/XIS spectrum of the potential X-ray counterpart of 1FGL J2017.3+0603 with the best fit power-law model. FI data are shown black, and BI data in gray.

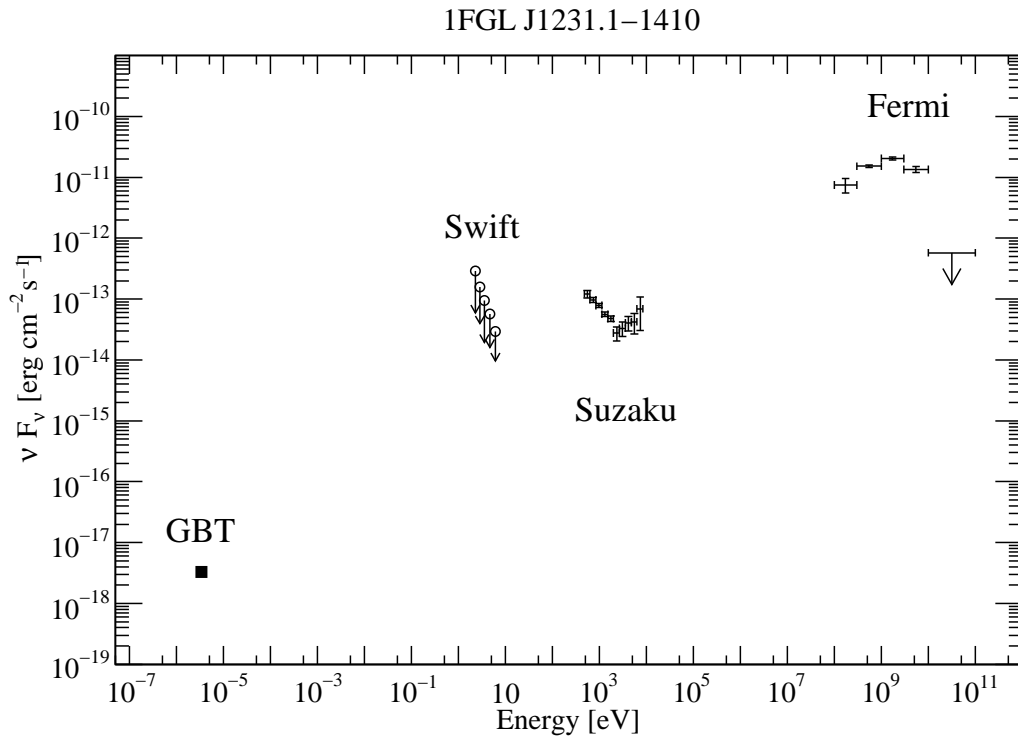


Fig. 13.— Broad-band spectrum of 1FGL J1231.1–1410/PSR J1231–1411. The X-ray data points represent the weighted mean of *Suzaku*/XIS FI and BI data. The  $\gamma$ -ray data points are taken from the 1FGL catalog (Abdo et al. 2010c). The radio data point is derived from the MSP PSR J1231–1411 observed with Green Bank Telescope by Ransom et al. (2010). The optical/UV upper limits were derived from the *Swift*/UVOT observation



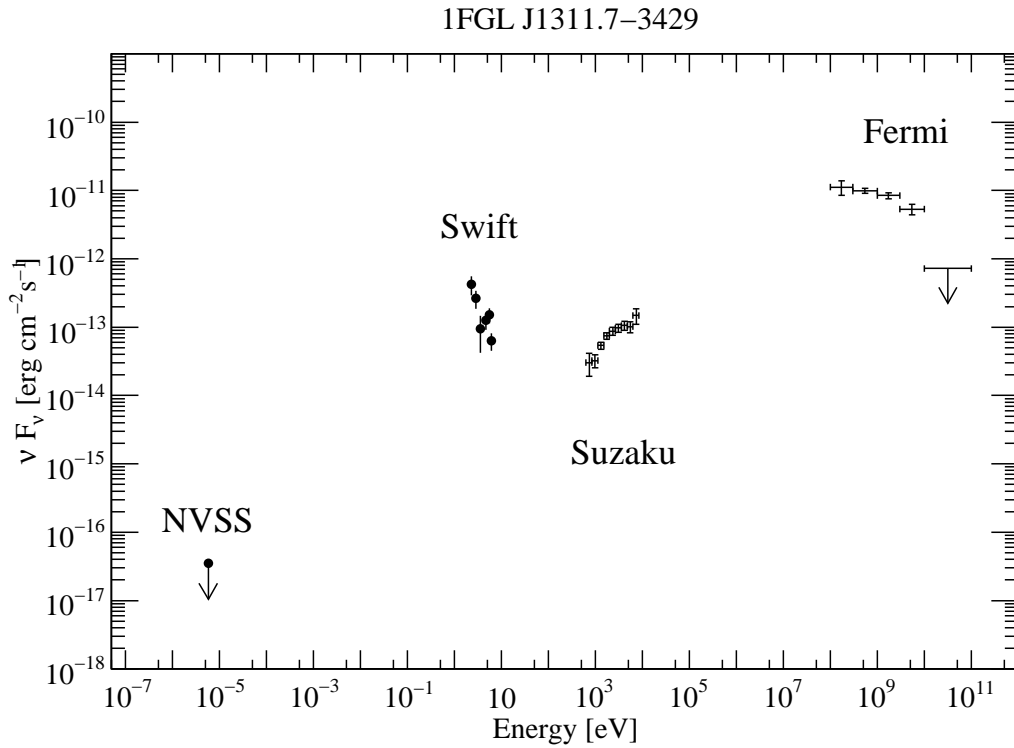


Fig. 14.— Broad-band spectrum of 1FGL J1311.7–3429. The X-ray data points represent the weighted mean of *Suzaku*/XIS FI and BI data for src A. The  $\gamma$ -ray data points are taken from the 1FGL catalog (Abdo et al. 2010c). The radio upper limit is taken from the NVSS catalog (Condon et al. 1998). The optical/UV data points show the *Swift*/UVOT data.

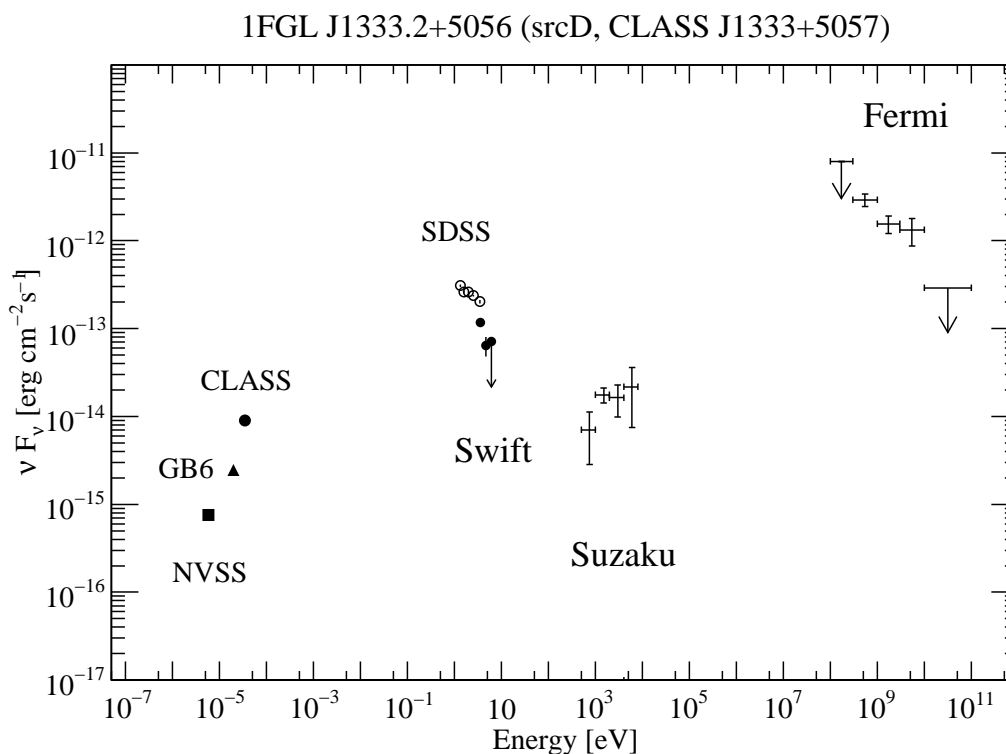


Fig. 15.— Broad-band spectrum of 1FGL J1333.2+5056/CLASS J1333+5057. The X-ray data points represent the weighted mean of *Suzaku*/XIS FI and BI data for src D which coincides with the CLASS source. The  $\gamma$ -ray data points are taken from the 1FGL catalog (Abdo et al. 2010c). The radio data points, representing blazar CLASS J1333+5057, are taken from the CLASS catalog (filled circle; Myers et al. 2003), NVSS catalog (filled square; Condon et al. 1998) and GB6 catalog (filled triangle; Gregory et al. 1996). Optical data point (open circle) was derived from SDSS J133353.78+505735.9 (SDSS Data Release 6; Adelman-McCarthy et al. 2008), optical/UV data points and upper limit (filled circle) is the *Swift*/UVOT data.

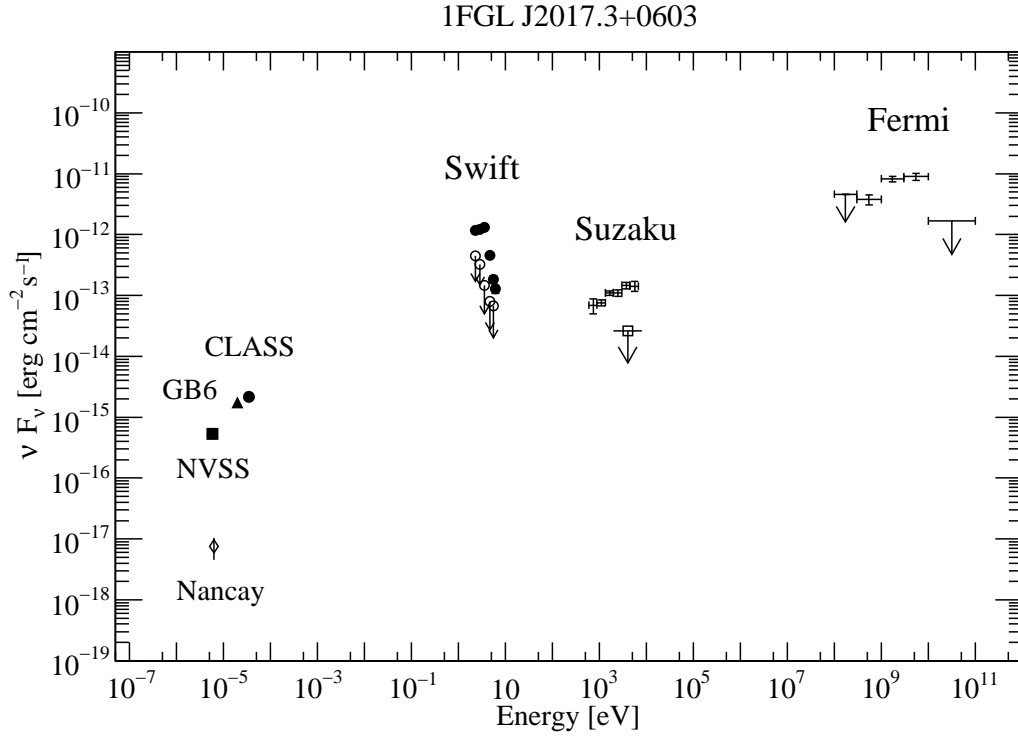


Fig. 16.— Broad-band spectrum of 1FGL J2017.3+0603. The X-ray data points represent the weighted mean of *Suzaku*/XIS FI and BI data for active galaxy CLASS J2017+0603. The X-ray upper limit (open square) is derived from the location of the MSP PSR J2017+0603. The  $\gamma$ -ray data points are taken from the 1FGL catalog (Abdo et al. 2010c). The radio data points, representing CLASS J2017+0603, are taken from the CLASS catalog (filled circle; Myers et al. 2003), NVSS catalog (filled square; Condon et al. 1998) and GB6 catalog (filled triangle; Gregory et al. 1996). The open diamond shaped point in radio shows the MSP PSR J2017+0603 observed with Nancay Radio Telescope (Cognard et al. 2010) and also the optical/UV upper limits (open circle) show the MSP observed with *Swift*/UVOT (Cognard et al. 2010). The optical/UV data points (corresponding filled circle) show the blazar CLASS J2017+0603 observed with *Swift*/UVOT.